The Astrophysical Journal, 696:328–347, 2009 May 1 doi:10.1088/0004-637X/696/1/328

FULL POLARIZATION SPECTRA OF 3C 279

D. C. Homan[1], M. L. Lister[2], H. D. Aller[3], M. F. Aller[3], and J. F. C. Wardle[4]
[1] Department of Physics and Astronomy, Denison University, 1 Main Street, Granville, OH 43023, USA; homand@denison.edu
[2] Department of Physics, Purdue University, 525 Northwestern Avenue, West Lafayette, IN 47907, USA; mlister@physics.purdue.edu
[3] Department of Astronomy, University of Michigan, Ann Arbor, MI 48109, USA; haller@umich.edu, mfa@umich.edu
[4] Department of Physics, Brandeis University, Waltham, MA 02454, USA; wardle@brandeis.edu
Received 2008 October 21; accepted 2009 February 11; published 2009 April 14

ABSTRACT

We report the results of parsec-scale, multifrequency Very Long Baseline Array observations of the core region of 3C 279 in Stokes *I*, linear polarization, and circular polarization. These full polarization spectra are modeled by radiative transfer simulations to constrain the magnetic field and particle properties of the parsec-scale jet in 3C 279. We find that the polarization properties of the core region, including the amount of linear polarization, the amount and sign of Faraday rotation, and the amount and sign of circular polarization can be explained by a consistent physical picture. The base of the jet, component D, is modeled as an inhomogeneous Blandford–Königl style conical jet dominated by a vector-ordered poloidal magnetic field along the jet axis, and we estimate its net magnetic flux. This poloidal field is responsible for the linear and circular polarization from this inhomogeneous component. Farther down the jet, the magnetic field in two homogeneous features is dominated by local shocks and a smaller fraction of vector-ordered poloidal field remains along the jet axis. This remaining poloidal field provides internal Faraday rotation which drives Faraday conversion of linear polarization into circular polarization from these components. In this picture, we find the jet to be kinetically dominated by protons with the radiating particles being dominated by electrons at an approximate fraction of $\gtrsim$75%, still allowing the potential for a significant admixture of positrons. Based on the amounts of Faraday conversion deduced for the homogeneous components, we find a plausible range for the lower cutoff in the relativistic particle energy spectrum to be $5 \lesssim \gamma_l \lesssim 35$. The physical picture described here is not unique if the observed Faraday rotation and depolarization occur in screens external to the jet; however, we find the joint explanation of linear and circular polarization observations from a single set of magnetic fields and particle properties internal to the jet to be compelling evidence for this picture.

Key words: galaxies: active – galaxies: individual (3C 279) – galaxies: jets – radiation mechanisms: non-thermal – radio continuum: galaxies

1. INTRODUCTION

The three-dimensional magnetic field structures and the particle populations of extragalactic jets from active galactic nuclei (AGNs) are still not well understood. Laing & Bridle (2002) and Laing et al. (2006) have recently made progress in studying the three-dimensional magnetic field structures of kiloparsec-scale jets, but little is known about the three-dimensional field structure near the jet origin, on parsec or subparsec scales. We wish to know if the jet magnetic field shows a structure which has its roots in the magnetic field in the supermassive black-hole/accretion-disk system responsible for giving rise to the jets (e.g., Blandford & Znajek 1977; Meier et al. 2001; Koide et al. 2002; Vlahakis & Königl 2004). Marscher et al. (2002) had suggested a direct disk–jet connection on the basis of X-ray/radio correlations, and this connection may extend to the magnetic field which threads the accretion disk around the black hole. Unanswered questions include, for example, is there significant vector-ordered poloidal field along the jet axis or perhaps a toroidal/helical field structure confining the jet and indicating a jet current (Asada et al. 2002; Gabuzda et al. 2004; Fendt 2006)? It is also unknown whether the particle population of jets is primarily electron–proton, p^+e^-, or electron–positron, e^+e^- (e.g., Wardle et al. 1998; Sikora & Madejski 2000; De Young 2006). We parameterize this unknown as the lepton number, $\ell = (n_- - n_+)/(n_- + n_+)$, where n_- and n_+ are the number densities of electrons and positrons, respectively. Additionally, the limits on the power-law particle spectrum which gives rise to the observed synchrotron radiation are poorly constrained. The relativistic number density can be parameterized as $N_\gamma d\gamma = K\gamma^{-p}d\gamma$ for $\gamma_l \leqslant \gamma \leqslant \gamma_u$ where it is assumed to have a hard cutoff to the power law at both high and low energies. Celotti & Fabian (1993) found that the lower cutoff γ_l set the scale for the bulk kinetic luminosity of jets because the low-energy particles dominate the particle density.

With submilliarcsecond resolution, Very Long Baseline Array (VLBA) observations of extragalactic radio jets can study synchrotron emission from jets within a few parsecs of the jet origin. Measurements of linear polarization from milliarcsecond jets are sensitive to the net magnetic field order in the plane of the sky; however, multiple three-dimensional magnetic field structures can all yield the same observed linear polarization. For example, a transverse shock of tangled magnetic field, a toroidal field, or a high-pitched helical field will all produce linear polarization with the electric field vector parallel to the jet axis. Likewise, a vector-ordered poloidal field, shear in a tangled field, or a low-pitch helical field will all produce linear polarization with the electric field vector transverse to the jet axis. Faraday rotation of linear polarization is sensitive to magnetic field order along the line of sight and to the properties of the particles doing the rotation. The observed Faraday rotation must, in some cases, result from thermal particles and magnetic fields which are along the line of sight but external to the jet, but for rotations smaller than about 45°, it is difficult to distinguish internal from external Faraday rotation without additional information (Burn 1966). Recently, several authors have attributed Faraday rotation gradients observed approximately transverse to jets as evidence of toroidal or helical magnetic fields either in the jet itself or in

a sheath layer around the jet (Asada et al. 2002; Gabuzda et al. 2004; Zavala & Taylor 2005; Attridge et al. 2005; Gómez et al. 2008); however, these gradients are often gradients in magnitude of a single sign of the observed rotation and do not show the clear antisymmetric signature expected for such fields, so an additional external Faraday screen must be proposed as well. Alternatively, the observed gradients in rotation measure could be due to density gradients in the material surrounding the jet. In the case of 3C 273, the case for toroidal or helical fields is stronger as the same direction of the gradient is observed at multiple jet locations (Zavala & Taylor 2005; Attridge et al. 2005; Asada et al. 2008). Marscher et al. (2008) have also argued for helical field structure in BL Lacertae based on temporal rotations in linear polarization angle from the jet core region.

Parsec-scale observations of circular polarization from extragalactic jets provide additional constraints that can break some of the degeneracies inherent in linear polarization observations. Circular polarization may be generated either as an *intrinsic* component of the emitted synchrotron radiation or via Faraday *conversion* of linear polarization into circular polarization (e.g., Jones 1988). Like Faraday rotation, *conversion* is a birefringence effect; however, unlike rotation, conversion is much stronger in relativistic particles than thermal particles, and we do not expect significant Faraday conversion from magnetic fields and particles external to the jet (Jones & O'Dell 1977; Homan et al. 2001). In this way, circular polarization probes the jet magnetic fields and particles directly without modification from external screens.

Parsec-scale circular polarization observations of AGN jets have been reported by Wardle et al. (1998), Homan & Wardle (1999, 2003, 2004), Homan et al. (2001), Homan & Lister (2006), and most recently by Gabuzda et al. (2008). Most AGN jets appear to have less than ∼0.1%–0.2% circular polarization, with 10%–20% of jets detected at the level of ∼0.3%–1.0% of the Stokes *I* emission from or very near the base of the jet (or "jet core"). The highest levels of circular polarization detected are 2%–4% of the local Stokes *I* emission in the core region of the nearby radio galaxy 3C 84 (Homan & Wardle 2004) and in the intraday variable source PKS 1519−273 (Macquart et al. 2000). Single dish monitoring of circular polarization from AGN jets by the UMRAO has been ongoing since 2002 (Aller et al. 2003), and the Austrian Compact Telescope Array has studied the integrated circular polarization from AGN (Rayner et al. 2000). Circular polarization has also been observed in intraday variable sources, microquasars, low-luminosity AGNs, and the Galactic center (Bower et al. 1999, 2002; Brunthaler et al. 2001; Fender et al. 2000, 2002; Macquart et al. 2000; Sault & Macquart 1999). To date, no strong correlations have been found between the appearance of circular polarization and other source properties (Homan et al. 2001; Rayner et al. 2000; Homan & Lister 2006); however, the lack of strong correlations may simply be related to the small fraction of detected sources and the low levels of circular polarization in those objects. There is increasing evidence that at least some circularly polarized sources tend to have a preferred "handedness" of circular polarization (Komesaroff et al. 1984; Homan & Wardle 1999; Homan et al. 2001; Bower et al. 2002; Homan & Lister 2006) suggesting a persistent magnetic field structure is responsible for setting the sign of the observed polarization, although it is important to note that changes in sign have been observed in some cases (e.g., Aller et al. 2003).

To date, radiative transfer modeling of parsec-scale circular polarization has been at only one or two frequencies, limiting our ability to uniquely constrain physical jet properties. Wardle et al. (1998) preferred a model for 3C 279 where circular polarization was produced via Faraday conversion of linear into circular polarization and this conversion was driven by some internal Faraday rotation. Their results implied a low cutoff in the relativistic particle spectrum of $\gamma_l \leqslant 20$, suggesting the jet was dominated by electron–positron pairs to keep the jet's kinetic luminosity within reasonable bounds (e.g., Celotti & Fabian 1993). However, subsequent work by Ruszkowski & Begelman (2002) and Beckert & Falcke (2002) showed that some addition of thermal matter to the jet allowed a larger value for γ_l, reducing the need for an electron–positron-dominated jet. Homan & Wardle (2003, 2004) also preferred Faraday conversion models for PKS 0607−157 and 3C 84, respectively. Gabuzda et al. (2008) have linked the observation of transverse rotation measure gradients with parsec-scale circular polarization observations in a qualitative fashion to show that both observations are consistent with helical magnetic fields if all eight jets in their sample emerge from the south magnetic pole of the central engine.

To make progress on using parsec-scale circular and linear polarization observations of AGN jets to constrain their magnetic field structure and particle populations, we have embarked on a program to study the linear polarization, circular polarization, and Stokes *I* spectra of AGN jets at six frequencies with the VLBA. We call these "full polarization spectra" of AGN jets, as we use all four Stokes parameters to constrain radiative transfer models. We combine these single-epoch, parsec-scale data with integrated monitoring by the UMRAO at 4.8, 8.0, and 14.5 GHz. The first VLBA observations in this program took place in 2005 November for 18 jets. We detected strong circular polarization at multiple frequencies in three jets: 3C 84, 3C 279, and 3C 380. Here we report our results on 3C 279. Future papers will explore 3C 84 and 3C 380, as well as the sources in our sample with little or no detected circular polarization. In Section 2, we describe our observations, calibration, and Gaussian modeling of the core region of 3C 279 to obtain spectra for fitting. In Section 3, we describe a variety of possible models for producing circular and linear polarization in jets and then use analytical and computational radiative transfer models to fit the full polarization spectra obtained in Section 2. We discuss the results of the radiative transfer modeling in Section 4, and our conclusions appear in Section 5. Throughout the paper, we assume a cosmology where $H_0 = 70\,\mathrm{km\,s^{-1}\,Mpc^{-1}}$, $\Omega_M = 0.3$, and $\Omega_\Lambda = 0.7$, and so at the redshift of 3C 279 ($z = 0.538$), 1 mas corresponds to a projected linear scale of 6.34 pc.

2. OBSERVATIONS

2.1. VLBA Observations and Reduction

In 2005 November 17–20, we observed 18 AGN radio jets with the National Radio Astronomy Observatory's VLBA[5] at six frequencies: 8.01 GHz, 8.81 GHz, 12.35 GHz, 15.37 GHz, 22.23 GHz, and 24.35 GHz. The observations were recorded at each frequency in dual circular polarization with single-bit recording at four intermediate frequencies (IFs) of 8 MHz bandwidth for a total bandwidth of 32 MHz. The observations were made over a continuous 72 hr period to minimize the effects of source variability with each of three 24 hr segments devoted to a pair of frequencies: 8.0 and 22 GHz, 12 and 15 GHz, and 8.8 and

[5] The National Radio Astronomy Observatory is a facility of the National Science Foundation operated under cooperative agreement by Associated Universities, Inc.

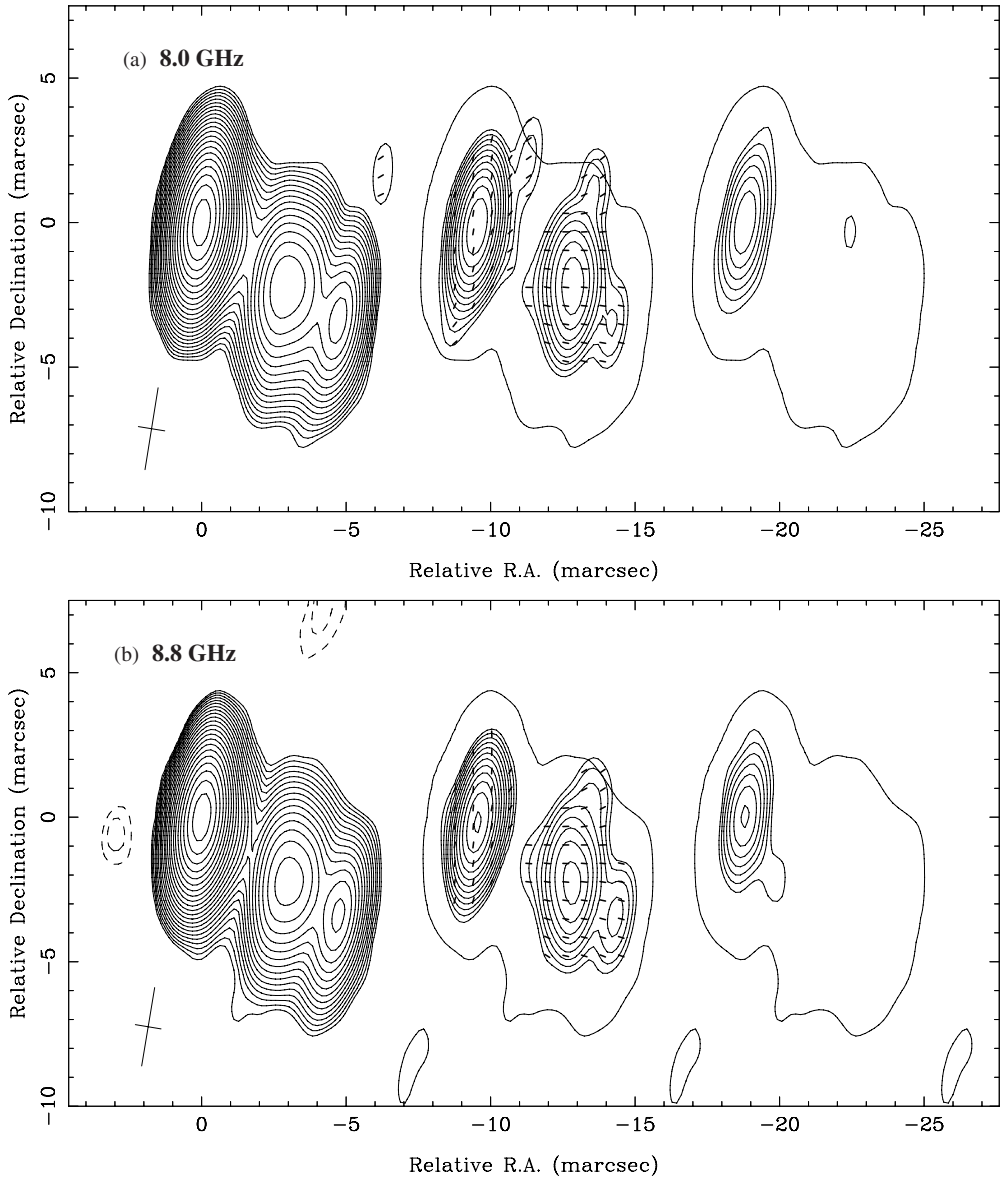

Figure 1. Contour images of Stokes *I* flux density (left), linearly polarized flux density (middle), and circularly polarized flux density (right) at 8.0 GHz (panel (a)) and 8.8 GHz (panel (b)). Contour levels begin at 5 mJy beam^{-1} for Stokes *I* and circular polarization, and 10 mJy beam^{-1} for linear polarization, and increase in steps of $\times\sqrt{2}$. Tick marks on the linear polarization image represent the measured EVPA. A single contour from the Stokes *I* image bounds the linear and circular polarization images to show registration. A cross-figure representing the FWHM dimensions of the restoring beam appears in the lower left-hand corner of each panel.

24 GHz, respectively. Each source was visited nine times at each observing frequency with these "scans" highly interleaved with neighboring sources to maximize (u, v) plane and parallactic angle coverage. Scan lengths were approximately 300 s at 22 and 24 GHz, 215 s at 12 and 15 GHz, and 130 s at 8.0 and 8.8 GHz. Each source thus obtained approximately 45 minutes integration time per frequency at 22 and 24 GHz, 32 minutes at 12 and 15 GHz, and 19 minutes at 8.0 and 8.8 GHz. Our calibrated Stokes *I* and polarization images at each of these frequency bands appear in Figures 1, 2, and 3, respectively.

A priori data calibration, fringe-fitting, self-calibration, and calibration for linear and circular polarization were performed at Denison University using the techniques described in detail by Lister & Homan (2005) and Homan & Lister (2006). At 15.4 GHz, the electric vector position angle (EVPA) of the linear polarization was calibrated by comparing to the MOJAVE database of rotated D-terms, as described in Lister & Homan (2005). At the other frequencies, we used the polarization of eight well-defined jet components and looked at their deviations from the 15 GHz calibration (which was taken as absolute); although there was some clear Faraday rotation in three of the components, the offsets at each frequency were remarkably consistent. We did make corrections for the apparent rotation measures of those three components, but our calibration is not strongly dependent on those values. Indeed, if we rely on only the five components without apparent Faraday rotation, we get the same calibration to within a degree at each frequency. Based on the scatter of the offsets between components, we estimate that our EVPA calibration is good to better than 1° at 12 GHz and below, and good to better than 2° at 22 and 24 GHz. These numbers are relative to the 15 GHz calibration, which we expect to be accurate to within 1° (Lister & Homan 2005); however, relative calibration between the frequencies is our main concern here for the modeling of the emission region. In our results,

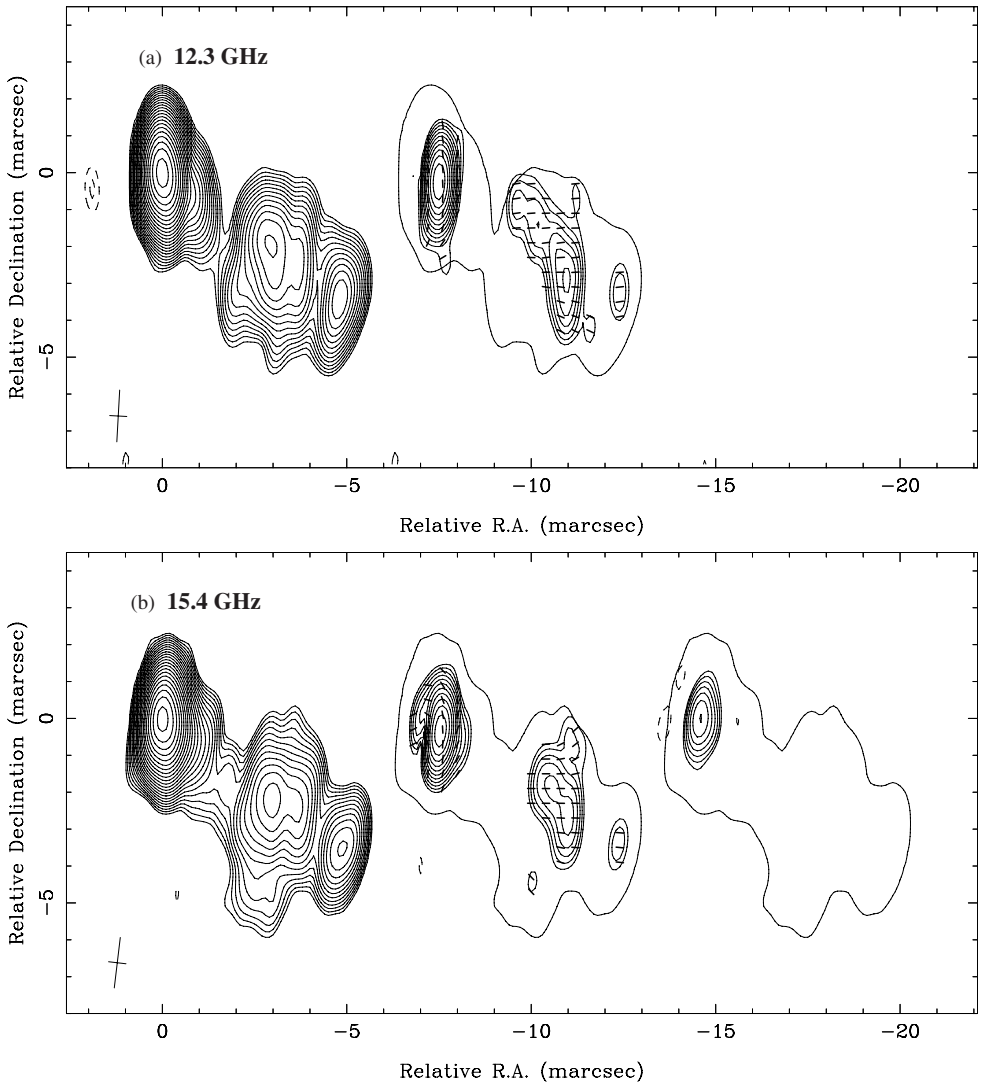

Figure 2. Contour images of Stokes *I* flux density (left), linearly polarized flux density (middle) and circularly polarized flux density (right) at 12.3 GHz (panel (a)) and 15.4 GHz (panel (b)). Contour levels begin at 5 mJy beam^{-1} for Stokes *I* and circular polarization, and 10 mJy beam^{-1} for linear polarization, and increase in steps of $\times\sqrt{2}$. Tick marks on the linear polarization image represent the measured EVPA. A single contour from the Stokes *I* image bounds the linear and circular polarization images to show registration. Note that severe RFI at 12.3 GHz prevented reliable measurement of the circular polarization at this frequency, so those data are not presented, see Section 2 for a more detailed description of this problem. A cross-figure representing the FWHM dimensions of the restoring beam appears in the lower left-hand corner of each panel.

we therefore consider only calibration uncertainty relative to 15 GHz added in quadrature with modeling uncertainty.

Circular polarization calibration was done via the gain transfer technique described in detail by Homan & Lister (2006), including their Monte Carlo methods to estimate the final uncertainty in the observed circular polarization. We have made some small improvements upon the methods described there to allow semi-automatic flagging of antennas and some individual scans that show a high right-circular polarization/left-circular polarization (RCP/LCP) gain ratio. In particular, we flagged an antenna if the standard deviation of its RCP/LCP antenna gain ratio was more than twice the median standard deviation of all the antennas. This requirement only resulted in the flagging of the OV antenna at 8.0 GHz which had a very large (a factor of $\simeq$2) gain discrepancy between the right- and left-hand feeds. We also flagged individual scans if their RCP/LCP ratio deviated by more than five times the standard deviation from the smoothed gains. In practice, this accounted for a very small percentage, 0.1%–0.3%, of the overall scans being flagged. As described in Homan & Lister (2006), we also excluded sources with low signal-to-noise ratio (S/N), as indicated by large RCP/LCP gain fluctuations, or with apparently high levels of circular polarization, as indicated by a larger RCP/LCP gain offset from the smoothed gains, from contributing to the final smoothed gain-transfer table which would determine the overall circular polarization calibration.[6] These requirements excluded only between one and three sources from contributing to the final gain smoothing at each frequency, except at 24 GHz where seven sources were excluded, likely due to lower overall S/N at that frequency. Our circular polarization observations at 12 GHz were corrupted by strong radio frequency interference (RFI), likely from geostationary satellites passing within the telescope beam, so we do not report circular polarization results at that frequency.

[6] The formal limit on the RCP/LCP gain fluctuations for low S/N sources was if the source had a standard deviation larger than twice the median standard deviation of all sources. The formal limit for a source with large apparent circular polarization was 0.5%, as indicated by a systematic RCP/LCP gain offset of $\geqslant$0.005 from the smoothed gains.

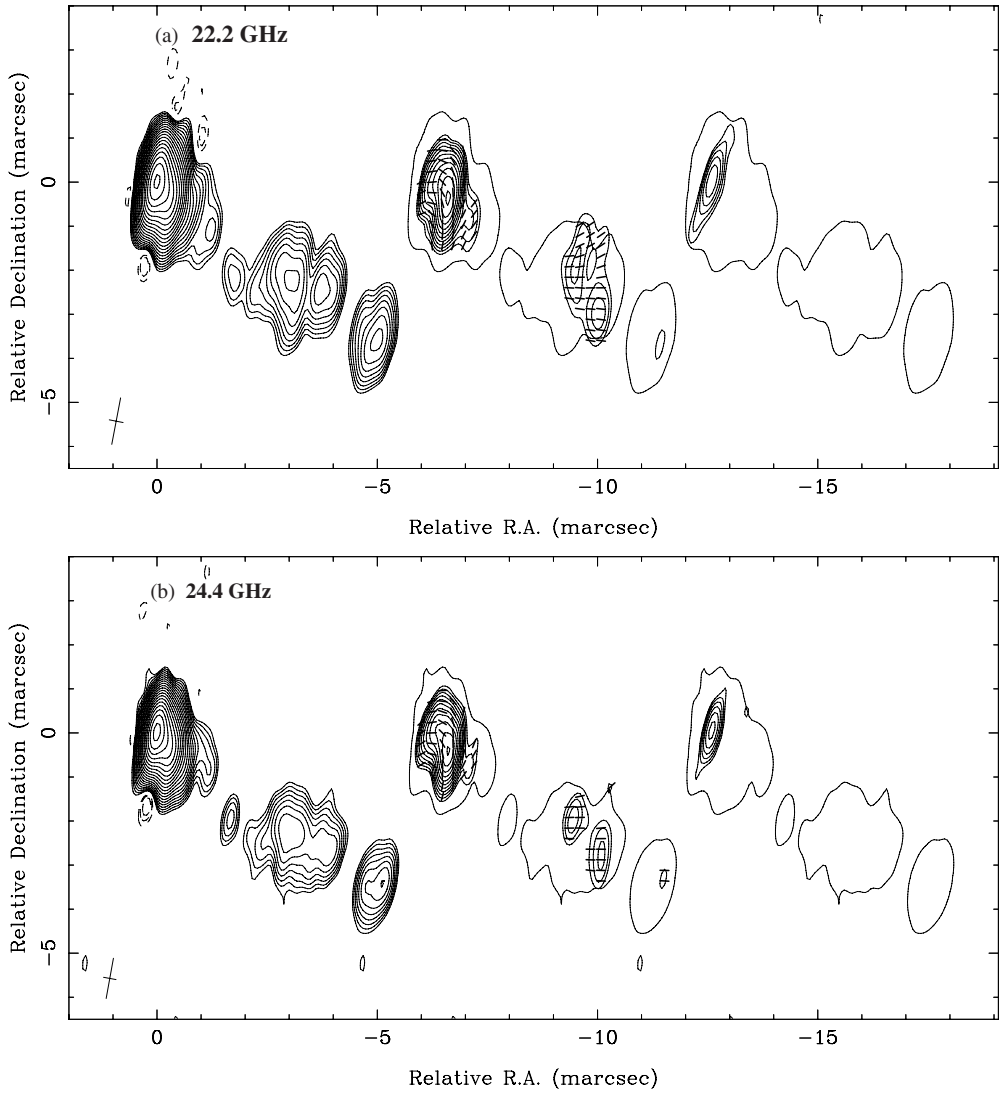

Figure 3. Contour images of Stokes *I* flux density (left), linearly polarized flux density (middle) and circularly polarized flux density (right) at 22.2 GHz (panel (a)) and 24.4 GHz (panel (b)). Contour levels begin at 10 mJy beam^{-1} and increase in steps of $\times\sqrt{2}$. Tick marks on the linear polarization image represent the measured EVPA. A single contour from the Stokes *I* image bounds the linear and circular polarization images to show registration. A cross-figure representing the FWHM dimensions of the restoring beam appears in the lower left-hand corner of each panel.

As discussed in detail in Homan & Lister (2006), phase calibration for circular polarization is complicated if a source has significant extended structure in Stokes *I*. This may lead to spurious antisymmetric structure in the resulting circularly polarized images due to phase errors in earlier steps in the calibration. To account for this effect, we use the same approach described and tested by Homan & Lister (2006) of adding an extra round of phase self-calibration, assuming no circular polarization in the data. In general, this extra round of phase self-calibration is very effective in removing genuine phase gain errors while preserving the original circularly polarized signal; although Homan & Lister (2006) did find that the amplitude of the circularly polarized signal may be reduced by a few percent up to 10% and the position of the circular polarization was shifted a small amount, less than about half a beamwidth, to better align with the source peak. Real circularly polarized structure significantly away from the source peak was not shifted by the procedure. In the case of a source with a broad core region, Homan & Lister (2006) found that the circular polarization may be spread by this procedure to encompass the whole region.

In recognition of the potential uncertainty of the precise placement of the circular polarization within the core region of 3C 279, we measured the integrated amount of circular polarization in the core region at each frequency using a single Gaussian component in the (u, v) plane, and these results are reported in Table 1.

As described below, the core region of 3C 279 is well modeled in Stokes *I* and linear polarization by three closely spaced components labeled D, 5, and 4 in Figure 4, and the third column of Table 1 shows the fractional circular polarization at each frequency if all of the measured circular polarization originated from component D. However, as described above, the complications of phase calibration for circular polarization limit our ability to confidently divide the measured circular polarization between these components at the lower frequencies, and indeed at 8.0 and 8.8 GHz, the measured circular polarization could come from any combination of these three components. At 15 GHz, the circular polarization is most likely associated with some combination of D and 5. At 22 and 24 GHz, we are confidently able to assign the measured circular polarization to

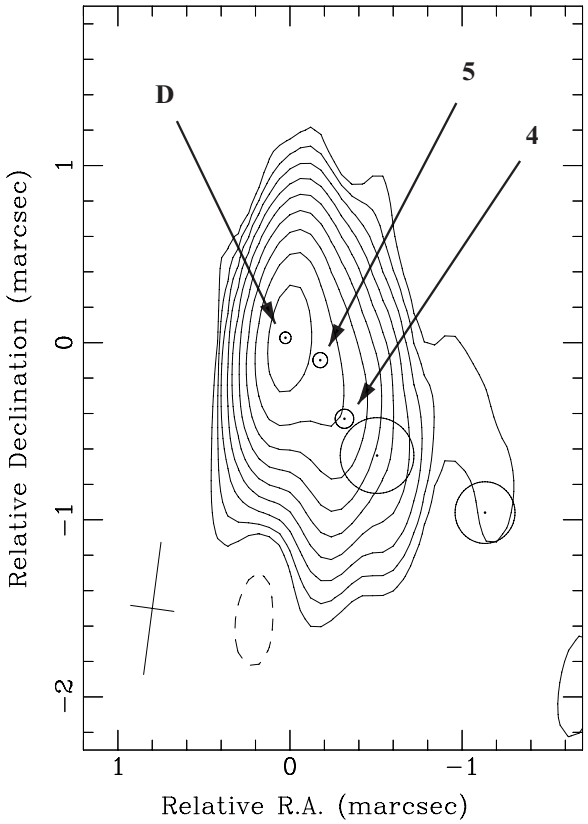

Figure 4. Uniformly weighted contour image of the core region at 24 GHz with the main core components labeled. Note that component positions and FWHM sizes plotted here are from a single possible set of model components. As described in the text, we fit seven possible sets of components to span a range of plausible scenarios for fitting the structure of this source. For example, the two weaker, unlabeled components in this figure are fit as a single component in two of our seven possible models.

Table 1
Circular Polarization of Core Region

Measured Values		If All Stokes *V* on "D"
Freq. (GHz) (1)	*V* (mJy) (2)	m_c (%) (3)
8.01	50.8 ± 9.6	1.99 ± 0.38
8.81	48.2 ± 8.0	1.55 ± 0.26
12.35	...	...
15.37	47.6 ± 7.9	0.88 ± 0.15
22.23	58.2 ± 13.4	0.86 ± 0.20
24.35	71.0 ± 16.5	0.94 ± 0.22

Notes. Columns are as follows: (1) frequency of observation in GHz; (2) Stokes *V* flux density for the core region in mJy; (3) fractional circular polarization under the hypothetical scenario, discussed in Section 3.4.1, where all the Stokes *V* flux is associated with component "D" in the core region.

component D at the base of the jet. To confirm this, we ran tests of our phase calibration procedure at 22 and 24 GHz by generating simulated data with the same Stokes *I* structure as the clean component models at these frequencies, but with the addition of a 10 or 20 mJy circularly polarized component at the locations of components 5 or 4 with the remaining circular polarization on component D. We found that the extra round of phase calibration assuming zero circular polarization was not able to move circular polarization that originated on components 5 or 4 to component D. These results give us confidence that the circular polarization observed on component D indeed originated on component D and was not transferred there by our phase calibration.

Table 2
Flux and Linear Polarization of Core Region Components

Component ID (1)	Freq. (GHz) (2)	*I* (Jy) (3)	m_l (%) (4)	χ (degrees) (5)
D	8.01	2.553 ± 0.301	3.3 ± 0.7	118.9 ± 4.0
	8.81	3.118 ± 0.304	3.9 ± 0.5	113.1 ± 1.7
	12.35	4.660 ± 0.441	3.0 ± 0.3	118.7 ± 2.7
	15.37	5.406 ± 0.393	2.5 ± 0.2	112.6 ± 3.1
	22.23	6.759 ± 0.431	2.4 ± 0.1	111.5 ± 3.1
	24.35	7.531 ± 0.476	2.2 ± 0.1	100.9 ± 2.8
5	8.01	3.914 ± 0.355	5.4 ± 0.8	18.1 ± 5.4
	8.81	3.865 ± 0.354	7.5 ± 0.9	19.9 ± 1.9
	12.35	3.944 ± 0.331	6.8 ± 0.8	37.4 ± 2.4
	15.37	3.329 ± 0.246	8.6 ± 0.6	41.6 ± 1.8
	22.23	2.812 ± 0.236	10.0 ± 0.9	49.3 ± 2.2
	24.35	2.977 ± 0.260	9.0 ± 0.8	48.8 ± 2.0
4	8.01	2.964 ± 0.433	13.3 ± 1.7	163.1 ± 3.3
	8.81	2.817 ± 0.397	13.5 ± 1.3	164.4 ± 2.1
	12.35	3.178 ± 0.313	13.5 ± 0.6	174.3 ± 1.5
	15.37	2.668 ± 0.228	16.3 ± 1.0	175.6 ± 1.2
	22.23	2.235 ± 0.157	16.6 ± 0.8	181.2 ± 2.2
	24.35	2.211 ± 0.160	16.3 ± 0.8	179.3 ± 1.9

Notes. Columns are as follows: (1) component identifier; (2) frequency of observation in GHz; (3) Stokes *I* flux density in Jy; (4) percent fractional linear polarization; (5) EVPA of linear polarization.

2.2. Gaussian Model of the Core Region

We used the Caltech Very Long Baseline Interferometry program *Difmap* (Shepherd 1997) to model the Stokes *I* structure and linear polarization of 3C 279 at each frequency with particular attention to the structure of the core region which produces the observed circular polarization. One challenge to this process is that the angular resolution of our observations differs by a factor of 3 between 8.0 and 24 GHz. To fit a comparable model over this range of resolution, we required that the relative separation, sizes, and shapes of the Gaussian components remain the same from one frequency to another; however, we allowed the fluxes of each component to vary as well as the overall phase center of the model.

One difficulty with this approach is that no single collection of model components will be ideal for all frequencies, so in total we repeated this process to fit seven separate sets of model components in this fashion. Each of these separate sets of model components explored somewhat different assumptions for how the structure of the core region and the remainder of the source was fit. For example, in some cases we fit elliptical Gaussians to the core region and in other cases circular Gaussian. We also tried varying the relative positions of the core components as well as the properties and numbers of components used to describe the rest of the jet. Taken together, these seven different sets of model components sampled a range of reasonable possibilities for fitting the structure of 3C 279. Overall the results for the core region were quite similar from one possibility to the next, and in Table 2 we report the average fluxes and polarizations from these different possibilities for each of the main core components. The uncertainties for the component properties given in Table 2 include calibration

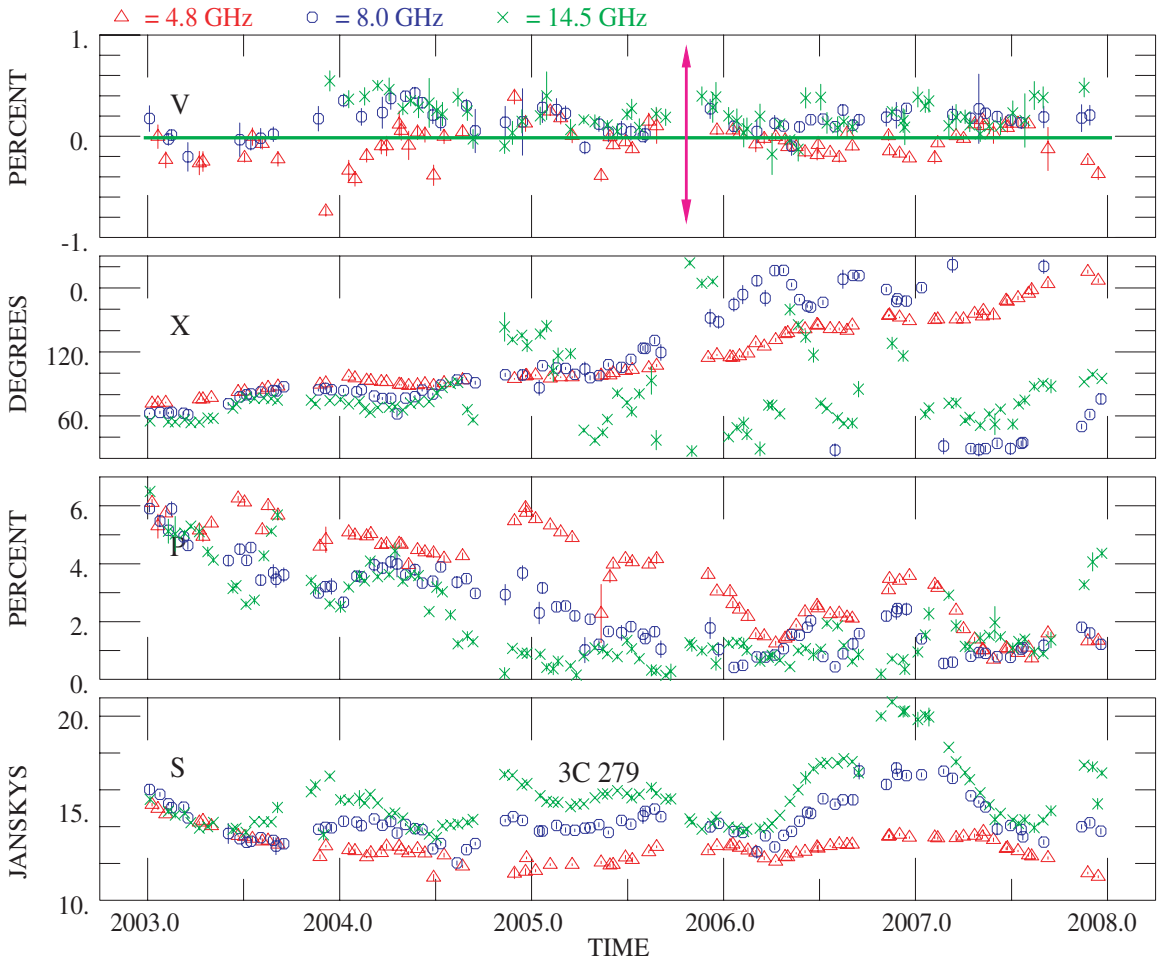

Figure 5. Integrated polarization monitoring by the UMRAO at 4.8, 8.0, and 14.5 GHz from 2003 through 2007. From the bottom to top, Stokes *I*, fractional linear polarization, EVPA, and fractional circular polarization. Two week averages of the data are shown. The standard errors, dominated by random measurement errors, are often smaller than the plotting symbols used. The horizontal line marks a zero level for circular polarization, and the vertical line indicates the epoch of the VLBA measurements.

uncertainties[7] added in quadrature with the standard deviation of the component values from the seven different sets of model components. Figure 4 shows the size and spacing of the three core region components from a representative set of model components.

2.3. UMRAO Integrated Monitoring of 3C 279

The integrated total flux density, linear polarization, and circular polarization of 3C 279 have been monitored with the University of Michigan 26 m telescope operating alternately at 4.8, 8.0, and 14.5 GHz. The prime-focus polarimeters, utilizing rotating quarter-wave plates feeding orthogonal linearly polarized transducers, measure all four Stokes parameters simultaneously. The general observing and calibration procedures used are described in Aller et al. (2003). Each series of on–off polarization observations, lasting approximately 40 minutes, was preceded by position scans to verify the pointing of the telescope. Observations of 3C 279 were interleaved with observations of reference sources at roughly 2 hr intervals. The instrumental polarization was checked from observations of bright galactic H II regions which are assumed to be unpolarized. All observations are restricted to within 3 hr of the meridian to minimize possible instrumental effects at large hour angles. Sources are not observed within 15° of the Sun at 14.5 or 8.0 GHz or within 30° of the Sun at 4.8 GHz to avoid solar interference. Because of these restrictions, there are annual gaps in the data for 3C 279 during September through mid-November at 4.8 GHz and from late-September through late-October at the two higher frequencies. Figure 5 shows the integrated emission of 3C 279 from 2003 through 2007. The annual gaps in the data are due to the close proximity of the Sun at those times. We detect nonzero circular polarization at all three observing frequencies, and within the measurement uncertainties the Michigan instrument measured the same amplitude and polarity of circular polarization as observed by the VLBA. During the period shown, circular polarization exhibited a preference to be negative at 4.8 GHz and positive at the two higher frequencies.

3. DERIVING PHYSICAL PARAMETERS OF THE EMISSION REGIONS

Our objective in this section is to model the magnetic field structure and particle properties in the core region of the parsec-scale jet of 3C 279. Tables 1 and 2 provide a large number of constraints: Stokes *I* spectra for each component, fractional linear polarization (LP), m_L, as a function of frequency for each component, EVPA, χ, as a function of frequency for each component, and finally, fractional circular polarization (CP), m_c,

[7] The overall flux calibration at each frequency was assumed to be good to 5% based on the results reported in the Appendix of Homan et al. (2002).

for the entire core region at low frequency and for component "D" at high frequency.

In the analysis that follows, we take the jet to have a bulk Lorentz factor of $\Gamma = 15$ at an angle of $\theta = 1.^{\circ}5$ to the line of sight, giving a Doppler factor of $\delta = 26$ for the jet. These numbers are consistent with the recent kinematical analysis of Homan et al. (2003). Similar but slightly larger values are found by Jorstad et al. (2004): $\Gamma = 20$ and $\theta = 1^{\circ}$, giving $\delta = 36$. Both sets of values give an observed angle in the frame of the emitting fluid of $\theta' \simeq 40^{\circ}$, and our results are not strongly dependent on which set of values we choose. If we did choose the "larger" value for the Doppler factor, it becomes somewhat easier to produce circular polarization via the intrinsic mechanism, as the estimated field strengths derived for the emission regions are somewhat larger (see Section 3.3).

3.1. Major Models of CP Production

Before we begin the detailed analysis, we will briefly outline five major models of circular polarization production which may be relevant to this source (e.g., Wardle & Homan 2003, and references therein).

Model (1) is stochastic production of circular polarization from a purely tangled magnetic field. In this model, the CP could be produced by either the intrinsic or Faraday conversion mechanisms, or some combination of the two. This model requires a fairly coarse-grained magnetic field tangling to do the job, as the sign of the produced circular polarization will differ from cell-to-cell, leading to square-root $-N$ style cancellation. A key prediction of this model is that the circular polarization should vary in sign and amount across different frequencies, which probe different parts of the jet near optical depth equals unity. We would also expect in this model that the CP would vary with time as the details of the magnetic field tangling change as the jet flows outward. Our observations of 3C 279 clearly show a consistency of sign and magnitude of circular polarization across the frequency bands, and previous work (e.g., Homan & Lister 2006) has shown that 3C 279 has maintained the same sign of circular polarization at high frequency for a decade now despite having a fast flowing jet and several outbursts over that period. The UMRAO has also observed a consistent sign of positive CP in 3C 279 at 14.5 GHz from 2003 through 2007 (see Figure 5); however, the UMRAO also finds periodic switches to negative CP at 4.8 GHz which we discuss in Section 4 as a possible opacity effect. Based on these results, we conclude that stochastic production of CP in a random magnetic field is not a major mechanism producing the CP we see in 3C 279. In the analysis that follows, we will therefore assume that any tangled portion of the magnetic field in 3C 279 is tangled on a very short length-scale to minimize the production of stochastic CP and allow exploration of the contribution by organized magnetic fields.

Model (2) is intrinsic circular polarization from a strong, vector-ordered magnetic field, hereafter *intrinsic circular polarization*. Given the consistency across epoch and frequency in the observed circular polarization of 3C 279, the most plausible candidate for such a vector-ordered field in the jet is a poloidal field along the jet axis. We can estimate the strength of such a field. If the magnetic field were completely uniform (no reversals or tangling), the expected circular polarization would be of order $m_c \sim \sqrt{\nu_B/\nu_{\rm emit}}$ where $\nu_B = 2.8B$ MHz is the electron gyro-frequency and $\nu_{\rm emit} = \nu_{\rm obs}(1+z)/\delta$ is the emitted frequency (e.g., Wardle & Homan 2003). So for 1% CP at 22 GHz, the required magnetic field strength is about $B \sim 50$ mG. This is not an unreasonable field strength, and as we shall see in Section 3.4.2, is of the order of the estimated field strength in component "D."

It is important to note that the above estimate assumes not only a uniform magnetic field, but also that all of the emitting particles are electrons. This will be the case in a "normal" matter jet consisting of a pure electron–proton plasma. Allowing for the possibility of some admixture of electron–positron pairs, parameterized by the lepton number, ℓ, defined in the introduction, the fractional circular polarization is $m_c \propto \ell$ and the required field strength would scale as $B \propto \ell^{-2}$.

Model (3) is Faraday conversion of linear polarization into circular polarization driven by Faraday rotation, hereafter *rotation-driven conversion*. In this model the LP is produced by whatever magnetic field order is available in the jet, such as shocked or sheared magnetic field. However, that LP cannot be directly converted into CP by the same field order because there needs to be some offset between the position angle of the LP and the angle of the magnetic field doing the conversion. The angular offset is provided by internal Faraday rotation within the jet, and in this model, the Faraday rotation depth is relatively small so that the field at the front of the jet is converting the LP emitted by the back of the jet into some CP.

For this to be a consistent (not stochastic) process, the Faraday rotation must be provided by some vector-ordered field in the jet, probably a poloidal field along the jet axis as in model (2). Additionally, there must also be some preponderance of electrons in the jet relative to positrons, i.e., $\ell > 0$. However, the requirements for some vector-ordered field and some preponderance of electrons in the jet plasma are not nearly as strong as they are for model (2), where the CP is produced entirely by the intrinsic mechanism. Model (3) has the additional requirement of low-energy particles within the jet to produce the internal Faraday rotation, either due to a low cutoff, γ_l, in the relativistic particle power-law spectrum $N_\gamma d\gamma = K\gamma^{-p}d\gamma$ for $\gamma_l \leqslant \gamma \leqslant \gamma_u$ or due to the addition of some "cold," nonrelativistic thermal matter to the jet.

It is interesting to note that the similarity in requirements between models (2) and (3) means that they will often act together to at least some degree.

Model (4) is a high rotation depth version of model (3), proposed and investigated independently by Ruszkowski & Begelman (2002) and Beckert & Falcke (2002). The requirements are almost the same as for model (3), but the rotation depth is much larger, so large, in fact, that significant rotation and conversion can happen over very small length scales in the jet. As long as this sense of rotation is common in all parts of the jet, no large-scale magnetic field order is required (except for the vector-ordered field which produces the rotation) and net circular polarization can be produced in potentially large amounts with little if any net linear polarization (Beckert & Falcke 2002; Ruszkowski & Begelman 2002).

Model (5) is Faraday conversion from a helical magnetic field or other field structure which varies systematically in orientation across the jet. In this model, no internal Faraday rotation is required, as the field orientation at the back of the jet is already at some angle with respect to the field orientation at the front of the jet (e.g., Wardle & Homan 2003).

3.2. Numerical Modeling

We have written a numerical simulation that solves the full-Stokes equations of radiative transfer (Jones & O'Dell 1977; Jones 1988) either by numerical integration or, optionally, by

using the exact solutions calculated by Jones & O'Dell (1977). An early version of this simulation was used by Wardle et al. (1998) to interpret the first parsec-scale circular polarization observations on 3C 279. The simulation models the emission from a "homogeneous" line of sight broken into cells where each cell has the same physical properties, including spectral index, α, lepton number, ℓ, Doppler factor, δ, viewing angle, θ, and low-energy power-law cutoff for the relativistic particle distribution, γ_l. The exception to this is the magnetic field, which may consist of multiple components which can vary in direction and/or magnitude from cell to cell depending on the magnetic field model applied. Additionally, multiple lines of sight can be put together to construct simple inhomogeneous models (see Section 3.4.2) or homogeneous models where the magnetic field has transverse structure, such as toroidal or helical magnetic fields (see Section 3.4.1). By adjusting the physical parameters and magnetic field model applied, we can simulate any of the five conceptual models described in the previous section. The radiative transfer is done in the frame co-moving with the fluid, and here we have assumed a single flow velocity where the relativistic flow parameters are derived from observed pattern speeds for this jet given by VLBA kinematical analyses as described in the introduction to this section. This simulation is static in the sense that the magnetic field and particle properties of the emission region are assumed not to change during a light crossing time.

3.2.1. Parameterization of the Magnetic Field

The magnetic field in our simulation can have three different components: a vector-ordered uniform field along the jet axis, $B_u = B_\star \times f_u$, a toroidal field, $B_t = B_\star \times f_t \times (\rho/\rho_{\rm jet})$, and a randomly ordered field which varies stochastically from cell to cell, $B_r = B_\star \times (1 - f_u - f_t)$. Here $B_\star$ is a scaling factor which allows us to match a desired average perpendicular magnetic field strength, $\langle B_\perp \rangle$, set by observation, f_u and f_t parameterize the degree of uniform and toroidal fields, respectively, and $\rho/\rho_{\rm jet}$ is the fractional distance of a cell from the center axis of the jet, where $\rho/\rho_{\rm jet} = 1.0$ is a cell at the outside edge of the jet. This parameterization of the toroidal field assumes that the current carried by the jet is uniformly distributed. Note that nonzero values for f_u and f_t together will produce a helical field order.

In addition to the three field components described above, the magnetic field may also be shocked, by shortening unit length to length, $k \leqslant 1.0$. This shock is assumed to be a transverse shock, so the shortening occurs along the jet axis. The result is amplification of the magnetic field components transverse to the jet axis as described in detail in the Appendix of Wardle et al. (1994).

3.3. Modeling the Stokes I Spectra

Figure 6 shows the Stokes *I* spectra of components D, 5, and 4 and their total flux density along with analytical models for each component. The total core flux at 4.8 GHz is estimated by comparing quasi-simultaneous UMRAO integrated measurements at 4.8, 8.0, and 14.5 GHz to our VLBA measurements.

Components 5 and 4 are modeled analytically as homogeneous synchrotron sources, but when we fit their six-frequency spectra using the Stokes *I* data alone, we found that the spectral turnover frequencies, $\nu_{\rm peak}$ were not well constrained at low frequency (see the first line in Table 3 for both components 5 and 4). However, the fractional linear polarization of both components decreased with frequency in a manner consistent with turnover frequencies closer to 9.0 GHz for both components. To quantify this observation, we developed an analytical model of how fractional linear polarization, m_l, should decrease with increasing optical depth, including the possible effects of depolarization from internal Faraday rotation. This model is described in detail in the Appendix.

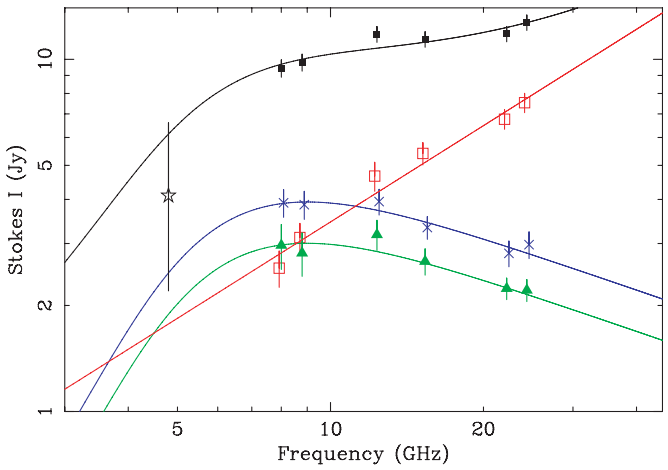

Figure 6. Stokes *I* spectrum of the core region of 3C 279. Component D is plotted with red open squares. Components 5 and 4 are plotted with blue × symbols and green filled triangles, respectively. The combined core region flux is plotted in black filled squares. An estimate for the combined core region flux at 4.8 GHz from comparison of the UMRAO and VLBA data is plotted as an open star. The spectral fits described in Section 3.3 are plotted as solid lines of the same color as the corresponding components.

Table 3
Spectral Turnover Fits to Components 5 and 4

Component ID	Method	$\nu_{\rm peak}$ (GHz)	$S_{\rm peak}$ (Jy)	α
(1)	(2)	(3)	(4)	(5)
5	Stokes *I* only	$8.95^{+1.83}_{-8.76}$	$3.94^{+4.99}_{-0.16}$	$-0.50^{+0.21}_{-0.20}$
	Stokes $I + m_l$	$9.51^{+0.63}_{-0.53}$	$3.93^{+0.20}_{-0.18}$	$-0.55^{+0.10}_{-0.09}$
	Stokes $I + m_l$ + FR	$8.61^{+0.77}_{-0.89}$	$3.93^{+0.24}_{-0.21}$	$-0.46^{+0.10}_{-0.10}$
4	Stokes *I* only	$10.21^{+1.11}_{-5.19}$	$3.06^{+2.07}_{-0.09}$	$-0.62^{+0.22}_{-0.22}$
	Stokes $I + m_l$	$9.23^{+0.86}_{-0.69}$	$3.00^{+0.23}_{-0.19}$	$-0.48^{+0.11}_{-0.10}$
	Stokes $I + m_l$ + FR	$8.94^{+0.95}_{-0.69}$	$3.01^{+0.24}_{-0.20}$	$-0.46^{+0.11}_{-0.11}$

Notes. Columns are as follows: (1) component identifier; (2) method of fitting spectral peak, as described in Section 3.3; (3) observed peak frequency in GHz; (4) peak Stokes *I* flux density in Jy; (5) spectral index.

We repeated the analytical fits including the fractional linear polarization data, both with and without the possibility of depolarization being due to the observed Faraday rotation being internal to the jet. The results for these more highly constrained fits are included in Table 3 and plotted in Figure 7, panels (a) and (b). To quantify the degree of observed Faraday rotation in these components we fit a regression of the standard form $\chi_{\rm obs} = RM\lambda^2 + \chi_{\rm emit}$ where we found $RM = -493 \pm 23$ rad m^{-2} and $RM = -250 \pm 25$ rad m^{-2} for components 5 and 4, respectively. These regressions are plotted in Figure 7, panel (c). Because the total rotations in these two cases are relatively small, a λ^2 regression works well regardless of whether the observed rotation is internal or external to the jet. For both components 5 and 4, our results, including or excluding the possibility of internal Faraday rotation, are consistent with peak frequencies of $\nu_{\rm peak} = 9.0 \pm 1.0$ GHz and spectral indices of $\alpha = -0.5 \pm 0.1$ (we use the convention $S \propto \nu^{+\alpha}$). Because our analysis is not particularly sensitive to the precise location of the turnover, we adopt these values in our subsequent analyses (they are also used to plot the spectra which appear in Figure 6).

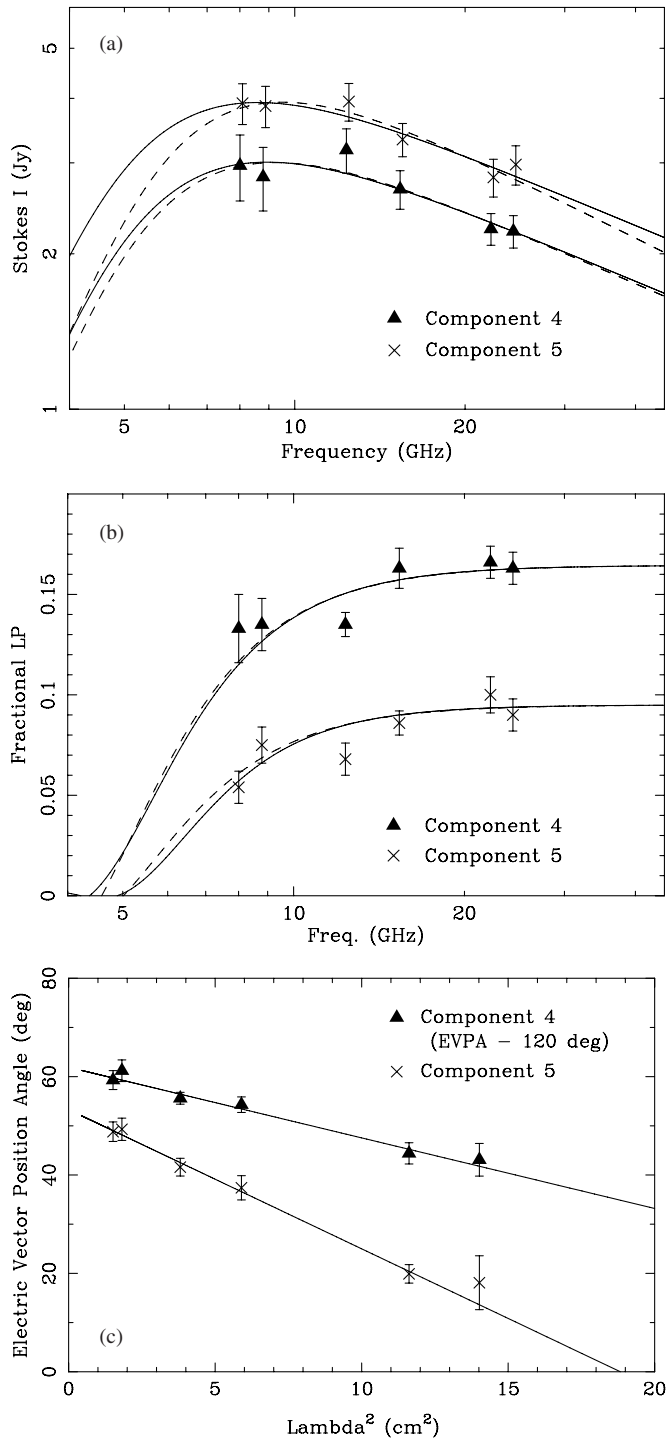

Figure 7. Stokes *I* (panel (a)), fractional linear polarization (panel (b)), and EVPAs (panel (c)) of components 5 and 4 plotted against two homogeneous spectrum models discussed in Section 3.3. The dashed lines in panels (a) and (b) represent a joint fit to the Stokes *I* and fractional linear polarization data assuming none of the observed Faraday rotation is internal to the jet. The solid line in these panels includes a modified Burn-style depolarization in the fit assuming that all of the observed Faraday rotation is internal to the jet. A λ^2 regression to the observed Faraday rotation is plotted in panel (c) as a solid line.

Component D has an inverted spectrum and is not well fit by a homogeneous source spectrum. It can be most simply fit by a straight power law with spectral index $\alpha = +0.91 \pm 0.08$. In Section 3.4.2, we will model component D as an inhomogeneous conical jet with power-law dependence on magnetic field strength and particle density as described by Blandford & Königl (1979) and Königl (1981).

3.3.1. Estimating Magnetic Field Strength

We can estimate the magnetic field strengths in components 5 and 4 by treating them as homogeneous spheres (e.g., Marscher 1987). For a homogeneous volume of plasma (Homan & Wardle 2000, Equation (A1))

$$B = \frac{\delta}{(1+z)} C_3 \tau_m^2 \nu_m^5 S_m^{-2} \Omega^2, \quad (1)$$

where $C_3 = 5.30 \times 10^{-4}$ for $\alpha = -0.5$, Ω in mas^2, ν in GHz, S in Jy, and B in Gauss. For a homogeneous sphere at the turnover frequency with $\alpha = -0.5$, $\tau_m = 0.48$, S_m is 1.19 times the observed flux S_o, and $\Omega = (\pi/6)\theta_d^2$, where θ_d is the angular diameter of the component (Homan & Wardle 2000). We use the approximation, $\theta_d \simeq 1.8(\theta_a \theta_b)^{-1/2}$, to convert Gaussian-fitted FWHM dimensions to spherical diameters (Marscher 1987).

Taking the median angular sizes fitted amongst our models, we estimate $B \sim 0.6$ mG for component 5 and $B \sim 4.4$ mG for component 4. These estimates depend on the assumed geometry and are probably only good to a factor of a few; however, our results are not strongly dependent on these values.

For the inhomogeneous component D, we can apply the above technique to make an order of magnitude estimate for its magnetic field strength; however, in that case, it would be more appropriate to take an optical depth τ between 1 and 2, and we estimate $\tau \sim 1.5$. Using the observed values at 22 GHz, we estimate $B \sim 40$ mG. In the following section, we will allow for a range of possible magnetic field strengths for component D.

3.4. Modeling the Polarization Spectra

3.4.1. Components 5 and 4

The Stokes *I* spectra of components 5 and 4 are adequately modeled by homogeneous components. Both features show strong linear polarization and modest amounts of Faraday rotation: $\simeq -35°$ to $-40°$ and $\simeq -15°$ to $-20°$ of total rotation by 8.0 GHz for components 5 and 4, respectively. We have no direct evidence for how much if any of this observed rotation is internal to the jet as neither of these rotations are enough to generate large amounts of internal depolarization. In the following analysis, we will construct two plausible models, one where all of the observed rotation is internal and the other where none of the rotation is internal to the jet.

Our observations indicate that very little, if any, of the observed circular polarization at 22 and 24 GHz is produced in these two features; however, by 8.0 and 8.8 GHz we cannot separate the circular polarization between D, 5, and 4. Indeed, if we assign all the circular polarization observed at 8.0 and 8.8 GHz to component D alone, we get very large levels of 1.99% ± 0.38% and 1.55 % ± 0.26%, respectively. These amounts are far larger than the amounts observed on D at 15, 22, and 24 GHz, where we find less than 1%. So, either component D must produce a sharp rise in circular polarization at these two frequencies, or components 5 and 4 make a significant contribution to the total circular polarization at 8.0 and 8.8 GHz but not at 15 GHz and above. To accomplish this second scenario, components 5 and 4 must each produce of order 0.5%–1.0% circular polarization at 8.0 GHz while producing $\lesssim$0.2% at 22 and 24 GHz.

In reference to the major models of circular polarization production considered in Section 3.1, only models (3) and (5) are plausible for these components. Model (2), intrinsic circular polarization, needs stronger magnetic field strengths and a higher degree of magnetic field order. Additionally, the spectral dependence of intrinsic CP, $m_c \propto \nu^{-0.5}$, is not steep enough. Model (4) requires very large rotation depths which are not observed here.

Model (3) from Section 3.1 is Faraday conversion driven by internal Faraday rotation, so for this model, we will assume that all of the observed rotation is internal to the jet. In this model, the magnetic field order which creates the linear polarization at the back of the jet is the same field order which does the conversion to circular polarization at the front of the jet. Faraday rotation within the jet rotates the linear polarization by angle ϕ to allow conversion by this same field, where the circular polarization produced is proportional to $\sin 2\phi$. So for this model to operate effectively, we need two components of organized magnetic field. The first component is in the plane of the sky and first produces the linear polarization and later converts it into circular polarization. The second component is vector-ordered magnetic field which produces the internal Faraday rotation.

For this model we will assume the first component of magnetic field is provided by a transverse shock. In component 5, the unrotated EVPA is approximately 54°, which gives a magnetic field position angle of −36°, nearly perpendicular to the structural position angle of −121° for component 5, indeed suggesting that the dominant field order is due to a transverse shock. For component 4, the unrotated EVPA is approximately 2°, giving a magnetic field position angle of −88° which is neither perpendicular nor parallel to its structural position angle of −143°, suggesting that the field order in component 4 is due to an oblique shock. Our radiative transfer simulation is set up to allow transverse shocks, see Section 3.2.1; however, for the purposes of simulating the effects of Faraday conversion in this model, the differences between an oblique and transverse shock are unimportant, as we only need the shock to provide field order in the plane of the sky to first produce the linear polarization and then to convert it into circular polarization.

For the second component of magnetic field which generates the internal Faraday rotation, we allow a vector-ordered field along the jet axis parameterized as $f_u = 0.05$ as described in Section 3.2.1 (note that $f_t = 0$ here so there is no contribution from a toroidal field component). With this degree of vector-ordered field along the jet axis, the shocks in components 5 and 4 must be of strength $k = 0.64$ and $k = 0.27$, respectively, to give the observed amounts of linear polarization at high frequency. We then put in the magnetic field strengths estimated in Section 3.3.1, and adjust the lower cutoff in the relativistic particle spectrum, γ_l, to give the observed amount of Faraday rotation: $\gamma_l = 19$ and $\gamma_l = 8.5$ for components 5 and 4, respectively. The optical depth at each frequency is set by the Stokes I spectra determined in Section 3.3. For each component, we assume a lepton number of $\ell = 1.0$, representing a pure electron–proton plasma. With these parameters set, we compute the radiative transfer along a line of sight with $N = 10^6$ cells to minimize stochastic effects from the random components of the magnetic field. The results of this calculation appear in Figure 8.

This model produces the correct sign, amount, and spectrum of circular polarization that we need for components 5 and 4, with m_c in the range of +0.5% to +1.0% at 8.0 GHz and falling off to negligible values at high frequency. An important question is: how sensitive are these values to the parameters chosen in the paragraph above? In short, these values are sensitive only to one parameter: the amount of internal Faraday rotation. In the above model, we have assumed that all of the observed Faraday rotation is internal to the jet. For modest optical depths, the circular polarization produced by Faraday conversion driven by Faraday rotation is proportional to the degree of magnetic field order squared, which is fixed by the observations of the linear polarization, and to the product $\tau_F \tau_C$, where $\tau_F = \zeta_V^* \tau$ and $\tau_C = \zeta_Q^* \tau$ are the Faraday rotation and conversion depths, respectively (Wardle & Homan 2003; Jones & O'Dell 1977).

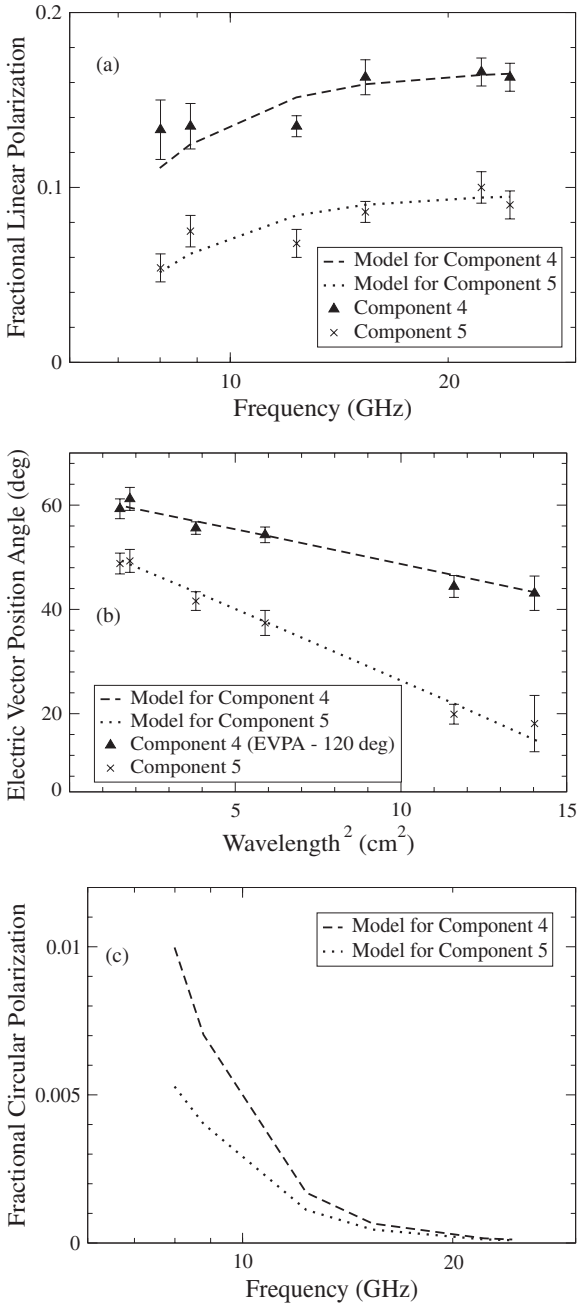

Figure 8. Linear and circular polarization spectra for components 5 and 4 from the rotation-driven conversion model described in Section 3.4. Panel (a) plots the fractional linear polarization model against the data, panel (b) plots the EVPA against the data, and panel (c) plots the predicted fractional circular polarization as a function of frequency. The model EVPA values in panel (b) have been shifted by a constant offset to align with the high frequency data. Note that in panel (b), the EVPA for component 4 has been shifted by −120° to allow it to fit comfortably on this plot.

The optical depth, τ, is also fixed by observation, so it is only the coefficients which matter. For $\alpha = 0.5$, the coefficients are given by

$$\zeta_V^* \simeq \zeta_\alpha^{*V} \ell f_u \frac{\nu}{\nu_{B\perp}} \frac{\ln \gamma_l}{\gamma_l^3} \cot\theta' \tag{2}$$

and

$$\zeta_Q^* = 2\zeta_\alpha^{*Q} \ln \frac{\gamma}{\gamma_l}, \tag{3}$$

where $\gamma = \sqrt{\nu/\nu_{B\perp}}$ is the γ of the radiating particles, and ζ_α^{*Q} and ζ_α^{*V} are constants of order unity. Note that the dependence on f_u given for ζ_V^* is approximate and only good for small values of $f_u \lesssim 0.1$.

In summary, if all of the observed Faraday rotation is assumed to be internal, then τ_F is also fixed by observation and the combination of parameters $\ell f_u B_\perp^{-1} \ln \gamma_l / \gamma_l^3$ is likewise fixed. Thus, the only place where parameter choice affects the results of this model is through the conversion depth τ_C which depends only weakly on the magnetic field strength, $B_\perp$ and the lower cutoff, γ_l, through the logarithm $\ln(\gamma/\gamma_l)$. In this respect, the rotation-driven conversion model is attractive as the sign, amount, and spectrum of circular polarization produced is nearly fixed by the observed properties of the linear polarization.

In contrast, the helical magnetic field model, model (5) from Section 3.1, has fewer constraints because here we assume that all of the observed Faraday rotation is external to the jet, so as to assess the ability of the helical field itself to produce the observed circular polarization. As above, we assume $f_u = 0.05$ for the vector-ordered component of magnetic field along the jet axis, and with this value, we require a toroidal field of $f_t = 0.56$ and $f_t = 0.78$ to match the observed levels of linear polarization in components 5 and 4, respectively. We note that the unrotated EVPA of component 4, computed above, is not consistent with a toroidal field which should be perpendicular to the jet axis; however, for the purpose of this analysis we will ignore this inconsistency.

With $f_t \gg f_u$, the overall field order is a high pitch-angle helix as suggested by Gabuzda et al. (2008) for 3C 279, and we can obtain similar levels of circular polarization as the rotation-driven conversion model by choosing $\gamma_l = 20$ and $\gamma_l = 10$ for components 5 and 4, respectively. We have also taken $\ell = 10^{-5}$ to completely eliminate any internal Faraday rotation, and no shock has been assumed for either component, $k = 1.0$. For a helical field, where the field order varies across the jet cross-section, a single line of sight is not sufficient to determine the emergent polarization, so we take a $100 \times 100 \times 100$ cube and set to zero any cells outside a cylindrical jet cross-section. The emerging polarization for both components is plotted in Figure 9.

As with the rotation-driven conversion model, the helical field is able to produce circular polarization with the correct amplitude, sign, and spectra; however, the amount and sign of the produced circular polarization are no longer determined by the linear polarization and are the result of choices we made about field direction and the magnitude of γ_l. The spectrum of the circular polarization from the helical field falls off more slowly than for the rotation-driven conversion case, but the levels are small enough at 15 GHz and above to still be acceptable. This shallower spectrum is due to the fact that the helical field produces CP via pure Faraday conversion and depends only upon τ_C, whereas rotation-driven conversion depends on the product of $\tau_F \tau_C$ which includes two powers of the optical depth.

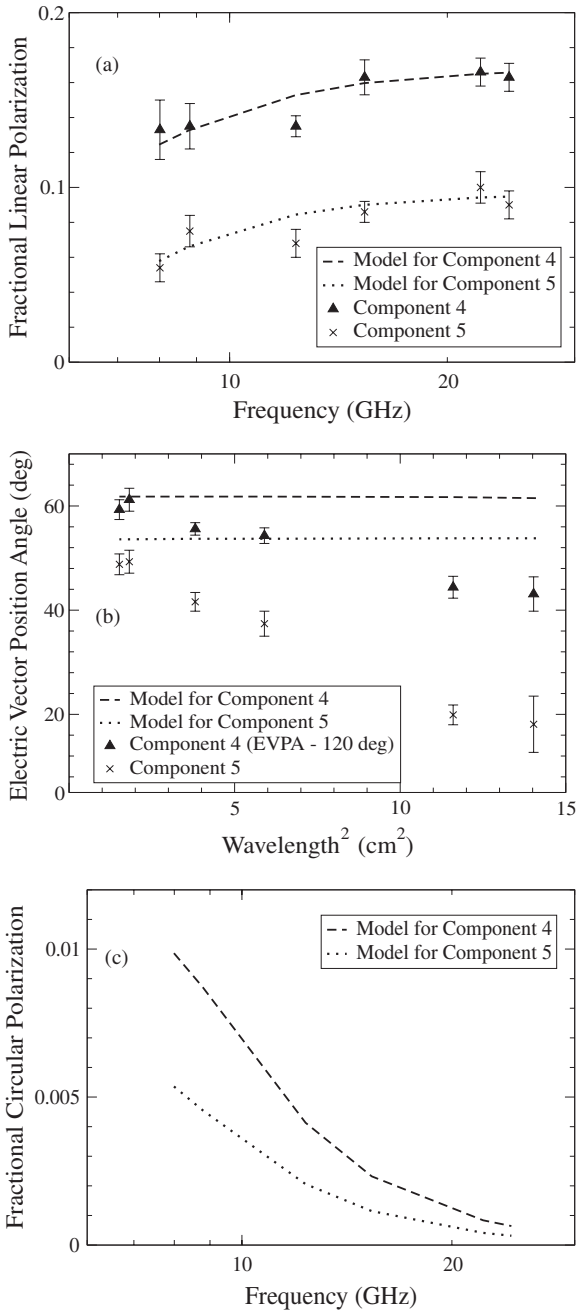

Figure 9. Linear and circular polarization spectra for components 5 and 4 from the helical field conversion model described in Section 3.4. Panel (a) plots the fractional linear polarization model against the data, panel (b) plots the EVPA against the data, and panel (c) plots the predicted fractional circular polarization as a function of frequency. The model EVPA values in panel (b) have been shifted by the same constant offset used in Figure 8. Note that in panel (b), the helical field model predicts a flat EVPA with frequency because none of the observed Faraday rotation is assumed to be internal to the jet. As in Figure 8, the EVPA for component 4 has been shifted by -120° to allow it to fit comfortably on this plot.

3.4.2. Component D

Component D represents the base of the jet as observed in our VLBA images, and it has an inhomogeneous spectrum which is well fit as a single power law $S \propto \nu^{+\alpha}$ where $\alpha = +0.91 \pm 0.08$ as described in Section 3.3. Its linear polarization is approximately flat or perhaps slightly decreasing with frequency from $m_l \simeq$ 3.6% to 2.3% from low to high frequency. The EVPA of the

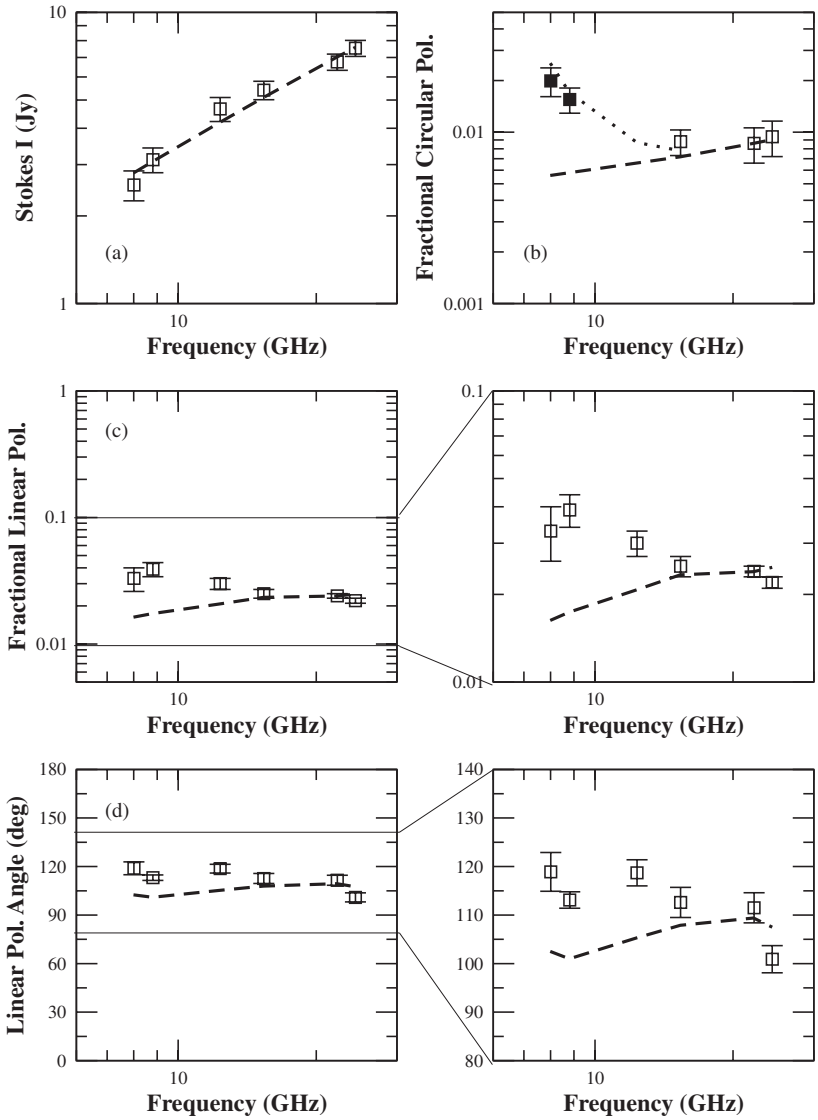

Figure 10. Full polarization spectra of the inhomogeneous component D. The data are plotted as open squares against a dashed line representing our best model described in Section 3.4.2. As described in that section the quality of the agreement was judged only at 15, 22, and 24 GHz; however, we plot the full spectrum here. Panel (a) is Stokes *I*. Panel (b) is fractional circular polarization. In panel (b), the 8.0 and 8.8 GHz values are plotted as solid squares to indicate that they may include significant contributions from components 5 and 4. The results from our rotation-driven conversion model in figure 8 are added to the inhomogeneous component D model and plotted as a dotted line in panel (b). Panel (c) is fractional linear polarization with a zoomed-in panel to the right to show agreement more clearly in the region of interest. Panel (d) is the EVPA with a zoomed-in panel to more clearly show agreement in the region of interest.

linear polarization stays roughly constant between +110° to +120° except for 24 GHz, where we find +101° ± 3°. Its circular polarization at 22 and 24 GHz is 0.86% ± 0.20% and 0.94% ± 0.22%, respectively, and if we assign all the observed circular polarization at 15 GHz to component D, we find a similar amount of 0.88% ± 0.15%.

These properties are all suggestive of an inhomogeneous component of the type investigated by Blandford & Königl (1979) and Königl (1981) where the magnetic field and particle densities scale as power laws in a conical jet with $B_\perp \propto r^{-m}$ and $K \propto r^{-n}$. The EVPA of the linear polarization described above corresponds to a jet magnetic field which is neither perpendicular nor parallel to the jet axis. The later is assumed to lie somewhere between the structural position angles of components 5 and 4 of −121° and −143°, respectively. Additionally, the observed levels of linear polarization at high frequency (2%–3%) are too low to generate the nearly 1% corresponding circular polarization if the linear polarization is taken as a direct measure of the field order. In all likelihood, Faraday rotation and depolarization, either internal or external to the jet, are responsible for the offset EVPAs and the low observed levels of linear polarization. If the culprit Faraday screen is external to the jet, then it must scale in a similar power-law fashion in order for the jet properties themselves to maintain an approximately constant level of depolarization and rotation with frequency. While such a scaling of an external screen is certainly possible, it seems more likely that the depolarization and rotation is occurring internal to the jet, where it naturally would scale in the appropriate manner with *B* and *K*.

In constructing our inhomogeneous model of component D, we will assume that all of the observed depolarization and rotation are occurring internal to the jet, matching our assumption for the rotation-driven conversion model of components 5 and 4. This assumption provides the most stringent constraints on component D, as the same magnetic field model must produce the correct signs and amounts of circular polarization, Faraday

rotation, and depolarization. From Section 3.1, models (2), (3), and (4) for circular polarization production all fit this scenario, and we can simultaneously investigate all three by constructing inhomogeneous jets consisting of vector-ordered field along the axis and disordered field which may be shocked from unit length to length k as described in Section 3.2.1.

We simulate conical, inhomogeneous jet emission by running our radiative transfer simulation for many lines of sight through the center of a jet where each line of sight corresponds to a new radius, r, from the base of the jet. The magnetic field strength and frequency where $\tau = 1$ are scaled at each radius, r, in a power-law fashion given by Königl (1981), where $B_\perp \propto r^{-m}$ and $\nu \propto r^{-k_m}$, where k_m is given by Königl (1981) and corresponds to a power-law scaling of not only $B_\perp$ but also the particle density, $K \propto r^{-n}$. In all of our models, we assume an optically thin spectral index of $\alpha = -0.5$. For $m = 1.8$ and $n = 2.8$, $k_m = 1.8$ and we find a good match to the Stokes I spectrum from our model. For these values, Königl (1981) would predict $S \propto \nu^{+0.89}$, which agrees well with our simulation. Other combinations of m and n could also match our Stokes I spectrum, and we explore three such combinations.

We set the magnetic field strength and degree of vector-ordered field at an observed frequency of 22 GHz. We require the vector-ordered field to scale like r^{-2} to conserve magnetic flux, and we adjust the scaling of the random component of the field to give the overall correct scaling for $B_\perp \propto r^{-m}$. For each location in the jet we compute the emerging radiation at our VLBA observing frequencies and integrate the results from the entire inhomogeneous component, cutoff at radii which produce low and high frequencies of 1 GHz and 100 GHz, respectively, in the observer frame. The Stokes I spectrum is then scaled by a single multiplicative factor, common to all frequencies, to best align with our observations. The model EVPA is also rotated by the same angle at all frequencies to best align with the observed EVPAs between 15 and 24 GHz; however, this angle is not arbitrary as it tells us the direction of the net magnetic field in the jet of 3C 279 and should correspond to a sensible value for the magnetic field model of the simulation. The final result is a model spectra of Stokes I, fractional linear polarization, EVPA, and circular polarization.

We initially ran a coarse grid of models with $m = 1.8$ and $n = 2.8$, exhausting all combinations of the following parameter values: $\ell = 1.0, 0.1, 0.01$, $f_u = 0.1$ to 0.9 in 0.1 steps, $B_\perp = 0.1, 0.05, 0.02, 0.01$ G, $\gamma_i = 3, 5, 8, 10, 15, 25, 50$, and $k = 0.1$ to 1.0 in 0.1 steps. We judged degree of agreement between model and data by comparing the fractional circular polarization, fractional linear polarization, and EVPA at 15, 22, and 24 GHz. We do not expect every variation and wiggle in the observed data to be reproduced by the inhomogeneous power-law models. In fact, we expect the inhomogeneous models to produce smoother-than-observed values for the polarization; however, we should be able to reproduce the general trends and levels observed. In this light, we required "plausible" models to produce an average circular polarization in the range $m_c = 0.8\%$–1.0%, with no value smaller than 0.6% or larger than 1.3%, and we required average linear polarization in the range $m_l = 2.2\%$–2.5%, with no value smaller than 2.0% or larger than 2.8%. These restrictions will only allow models to be plausible if they reproduce the general levels and slopes in the observed data. Out of more than 7000 models in this coarse grid, we found only two that fit these criteria; both models had $\ell = 1.0$, $B_\perp = 0.1$ G, $f_u = 0.7$–0.8, $\gamma_i = 5$, and $k = 0.8$–0.9.

Physically, these plausible models represent a jet dominated by vector-ordered magnetic flux along the jet axis, producing large amounts of internal Faraday rotation/depolarization with a significant contribution from intrinsic circular polarization as well as rotation-driven conversion. A range of similar models, while not meeting our plausible criteria did show similar trends in m_l and m_c, and we wished to explore this type of physical model with a finer grid. This new grid looked at every combination of $\ell = 1.0, 0.5, 0.1$, $B_\perp = 0.1, 0.05, 0.02, 0.01$ G, $f_u = 0.50$ to 0.95 in 0.05 steps, and $\gamma_i = 3, 4, 5, 6, 7, 8, 9, 10$. We realized that the shock strength, k, was not a physically meaningful parameter in this case, so we set $k = 1.0$ for our fine grid. Out of these 900+ models, we found four models meeting the plausible criteria discussed above. All of these models had $\ell = 1.0$, $B_\perp = 0.05$ G or 0.1 G, $f_u = 0.7$–0.9, and $\gamma_i = 5$ or 6. The best overall model from this set is plotted in Figure 10.

The model plotted in Figure 10 has $\ell = 1.0$, $B_\perp = 0.05$ G, $f_u = 0.8$, and $\gamma_i = 6$. While the comparison between model and data was done at 15 GHz and above, we show here the full spectra of the model at all our observing frequencies. Note that the model deviates from the fractional linear polarization and EVPA data below 15 GHz. This trend could be easily explained if the amount of internal rotation reduced more quickly than expected at larger r, perhaps due to local conditions in the jet or an increase in the lower cutoff to the relativistic particle spectrum, γ_i, with r. This deviation illustrates an important limitation of this model which can only simulate broad spectral trends from smoothly varying physical properties.

For the circular polarization at 15 GHz and below in Figure 10, we have added a dotted line which includes the contributions from the rotation-driven conversion models of components 5 and 4, given in Figure 8. Note that the total circular polarization at low frequency is approximately correct with this addition, although the total falls a bit higher than the measured 8.0 GHz value.

The intrinsic magnetic field direction in this model corresponds to a position angle of -129°, which places it between the structural position angles of components 5 and 4. This is consistent with a parallel magnetic field ordered along a jet axis which points at $\simeq -129^\circ$. All of our plausible models gave derotated magnetic field directions between -129° and -133° to give the best match to the 15, 22, and 24 GHz data. Given that all of these models are dominated by vector-ordered field along the jet axis, i.e., $f_u \geqslant 0.7$, this is an important consistency check, revealing that not only does this model produce the appropriate amounts of both linear and circular polarization, but it also produces approximately the right amount and sign of EVPA rotation for the emerging radiation.

To check our dependence on the power-law exponents, m and n, we repeated the coarse grid described above for two additional combinations, $m = 1.3$, $n = 3.4$ and $m = 2.3$, $n = 2.3$, both of which match our Stokes I spectrum. We found only one model which fit our plausibility criteria, and it had $m = 2.3$, $n = 2.3$, $\ell = 1.0$, $B_\perp = 0.02$ G, $f_u = 0.8$, $\gamma_i = 10$, and $k = 0.7$. The intrinsic magnetic field direction in this model corresponds to a position angle of -128°. These results present a very similar physical picture to the best models with $m = 1.8$ and $n = 2.8$.

4. DISCUSSION

4.1. Homogeneous Components 5 and 4

For components 5 and 4, we find little to no circular polarization at 22 and 24 GHz and as much as 0.5%–1.0%

circular polarization by 8.0 GHz. In Section 3.4.1, we explored two possible physical models to explain this circular polarization spectra both based on Faraday conversion of linear polarization into circular. The first model corresponds to model (3) described in Section 3.1, *rotation-driven conversion*, and involves linear polarization generated by a shocked magnetic field, a vector-ordered component of field along the jet axis which causes Faraday rotation of the linear polarization within the jet, and finally conversion of the rotated linear polarization into circular polarization by the shocked magnetic field. The results of this model were plotted in Figure 8. The second model corresponds to model (5) described in Section 3.1, conversion in a helical field, and involves linear polarization generated at the back of the jet being converted into circular polarization by the magnetic field at the front of the jet which is at some angle with respect to the field at the back of the jet.

Both of the models for components 5 and 4 described above are Faraday conversion models, as this will give the necessary steep spectrum, and both explain the circular polarization of these components adequately. However, we prefer the rotation-driven conversion model because it not only explains the circular polarization but also the linear polarization, including the amount and sign of the observed Faraday rotation. As described in Section 3.4.1, in this model the amount and sign of the observed circular polarization is essentially fixed by the amount of internal Faraday rotation along with the observed degree of magnetic field order given by the linear polarization. On the other hand, the helical field model has greater freedom to tune the amount and sign of the observed circular polarization because it decouples the observed Faraday rotation into an external screen which may have different properties than the jet itself.

If all of the observed Faraday rotation in components 5 and 4 is internal to the jet, the Faraday conversion depth at 8.0 GHz, τ_c, is constrained to lie in the ranges 1.5–3.0 and 0.75–1.5 for components 5 and 4, respectively, to generate fractional circular polarization in the range $m_c = 0.5\%$–1.0% for each component. For the observed optical depths of these components, the Faraday conversion depth constrains the Lorentz factor ratio between the emitting particles and the low-energy cutoff, γ/γ_l, to be in the range 20–400 for component 5 and in the range 4.5–20 for component 4. Using the estimated magnetic field strengths from Section 3.3.1 to find γ at 8.0 GHz, the lower cutoff in the particle energy spectrum is constrained to be $1 \lesssim \gamma_l \lesssim 27$ and $9 \lesssim \gamma_l \lesssim 43$ for components 5 and 4, respectively. Note that these limits scale with the estimated magnetic field strength like $1/\sqrt{B}$.

From the observed Faraday rotation itself, we obtain only a joint constraint on $f_u \ell \ln \gamma_l/\gamma_l^3$ as described in Section 3.4.1. If there is significant cold "thermal" matter inside the jet, this constraint will be modified by an additional term: $+R_c(3/4)/\gamma_l$, where R_c is the number ratio of cold to relativistic particles in the jet (Jones & O'Dell 1977).

4.2. Inhomogeneous Component D

The inhomogeneous component D lies at the very base of the parsec-scale radio jet, and we argue in Section 3.4.2 that its Stokes I and polarization spectra can be well modeled by a Blandford & Königl (1979) and Königl (1981) style conical jet with magnetic field and particle strengths that scale as power laws with distance from the jet origin. We prefer a physical model for component D where the linear polarization is depolarized and rotated by the same magnetic field and particles in the jet which produce the Stokes I emission, linear polarization, and circular polarization. These circumstances provide the strongest constraints on the physical properties of the jet magnetic fields and particles as these properties alone must produce consistent amounts and directions of both linear and circular polarization across multiple frequencies. The physical model required by these constraints is dominated by a vector-ordered magnetic field along the jet axis with $f_u \geqslant 0.7$ which does three things: (1) produces the observed linear polarization, (2) generates internal Faraday rotation which rotates the EVPA and depolarizes the linear polarization to the low fractional levels observed, and (3) produces the observed circular polarization largely as *intrinsic* circular polarization, although there is some contribution from *rotation-driven conversion* of the linear polarization into circular.

It is interesting to note that the dominant mechanism for producing circular polarization in components 5 and 4 is rotation-driven conversion, not intrinsic circular polarization; however, these homogeneous components are not dominated by vector-ordered magnetic field along the jet axis which would be required for efficient intrinsic circular polarization production. In fact, for components 5 and 4, some fraction of vector-ordered field, f_u, is required to generate the necessary internal Faraday rotation, and indeed *the same polarity* of vector-ordered field is required in components 5 and 4 as we deduce for component D.

4.2.1. Estimating the Jet Magnetic Flux

For our model of the inhomogeneous component D, we required the vector-ordered field to scale as r^{-2} along the jet axis, consistent with conservation of magnetic flux in a conical jet. Continued conservation of magnetic flux further down the jet in components 5 and 4 would leave some smaller fraction of vector-ordered field in these components with the same polarity. For components 5 and 4, it is not possible to compute the required magnetic flux because, as described in Section 4.1, f_u is tied to other unknown parameters, and it is also not clear whether components 5 and 4, which are on different structural position angles, occupy the entire jet width at their location or represent bright spots within a jet with a wider opening angle. However, these limitations do not apply to component D which has $f_u \geqslant 0.7$, and we can estimate the jet magnetic flux by fitting the transverse size of component D in our VLBA data. We find the transverse size to be in the range 0.02–0.04 mas; however, we note that we are at the very limits of our resolution here and can only use this value to estimate the jet magnetic flux. To convert from Gaussian FWHM to diameter of the jet, we multiply by 1.8 (Marscher 1987), and at a redshift $z = 0.536$, 1 mas corresponds to a linear scale of 6.3 pc for standard cosmological parameters of $H_0 = 70$ km s^{-1} Mpc^{-1}, $\Omega_M = 0.3$ and $\Omega_\Lambda = 0.7$. For $f_u = 0.7$ and $B_\perp = 0.050$ G, the net magnetic flux in the jet is in the range $\sim 2 \times 10^{34}$ to 1×10^{35} G cm^2.

This net magnetic flux is, to our knowledge, the first estimate of the magnetic flux carried by a jet that takes proper account of the vector order of the magnetic field. In the absence of field line reconnection or entrainment, it is a conserved quantity and is therefore equal to the net poloidal magnetic flux at the central engine. If the field originates in the black hole magnetosphere, then the expected magnetic flux for an Eddington black hole is $\sim 2 \times 10^{32} M_8^{3/2}$ G cm^2 (Wardle & Homan 2003, after correcting an arithmetic error; Begelman et al. 1984). Setting this equal to the measured magnetic flux implies a black hole mass in the range $\sim 2 \times 10^9$ to 6×10^9 $M_\odot$ in 3C 279. This would be at the top of the range of measured or inferred black hole masses

found in the literature (Woo & Urry 2002) but is not implausible; however, this estimate is an order of magnitude larger than the inferred black hole mass for 3C 279 itself (Woo & Urry 2002; Wang et al. 2004; Liu et al. 2006). Alternatively, the poloidal magnetic field may be anchored in the accretion disk, generally leading to larger magnetic fluxes because the area is much larger (e.g., Blandford & Payne 1982; Vlahakis & Königl 2004). In the latter paper, the net magnetic fluxes in the two models presented are 10^{34} G cm^2 and 10^{35} G cm^2 (N. Vlahakis 2008, private communication) which span our estimated range. The concordance between estimated and expected values suggests that circular polarization measurements can indeed measure a fundamental property of the central engine, and may even enable discrimination between models.

4.2.2. Jet Composition

The other physical parameter of interest constrained by this model is the lepton number ℓ, which we find to be 1.0 in all of our plausible models; however, the next smallest value we tested was $\ell = 0.5$. The lepton number is most strongly constrained by the circular polarization which is largely due to intrinsic circular polarization in this model. Smaller values of ℓ require larger values of B, such that $B \propto \ell^{-2}$, so if $\ell = 1.0$ for $B \simeq 0.05$ G as we find here, $\ell = 0.5$ would correspond to $B \simeq 0.2$ G.[8] Pushing this further, values as small as $\ell = 0.1$ might be allowed for stronger magnetic fields up to a few Gauss; however, larger values of B produce correspondingly larger values of the magnetic flux which is already quite large when estimated assuming $B = 0.05$ G, see Section 4.2.1. Additionally, from our observed flux density, angular size, and estimated optical depth at 22 GHz, we estimated $B \simeq 0.04$ G in Section 3.3.1, and while differing from this value by a factor of a few is certainly possible, the large deviations required for $\ell = 0.1$ or less are implausible. We therefore find that in this model, the jet in 3C 279 is at least dynamically dominated by protons with ℓ likely to be greater than or equal to about 0.5, corresponding to $\gtrsim$75% of the radiating particles being electrons.

In the first parsec-scale circular polarization study of 3C 279, Wardle et al. (1998) preferred a jet dominated by electron–positron pairs, and their argument was based on their conclusion that $\gamma_l \leqslant 20$ and therefore a jet dominated by electron–positron pairs was required by kinetic luminosity arguments originated by Celotti & Fabian (1993). Applying the same calculation as Wardle et al. (1998) for jet energy flux to these observations, we derive a similar constraint with $F_E = 1.33 \times 10^{45}[1 + 153\ell/\gamma_l]$ erg s^{-1}. This calculation assumes a magnetic field strength of $B_\perp = 0.05$ G and, like that of Wardle et al. (1998), assumes equipartition between the magnetic field and particle energies. Therefore, this calculation should be taken as a lower limit on the jet kinetic luminosity when the field strength is 0.05 G. Wardle et al. (1998) found a value for F_E about twice this, and they concluded that $\gamma_l \leqslant 20$ required a mostly electron–positron jet to avoid carrying much more energy than appears to be dissipated on larger scales. It should be noted that in our model here, because the field strength, B, scales roughly with ℓ^{-2}, reducing ℓ far below 1.0 does not reduce the energy carried by the jet, but rather increases it sharply as ℓ^{-4}.

It seems that in this picture for component D there are only two ways to reduce the energy carried by the jet in the calculation given above. The first is reducing the magnetic field strength, which is possible as we had at least one model with $B_\perp = 0.02$ G when we tried power-law indices of $m = 2.3$ and $n = 2.3$, as described in Section 3.4.2. The second is by increasing γ_l. As we noted in the introduction, work by Beckert & Falcke (2002) and Ruszkowski & Begelman (2002) showed that the addition of thermal plasma to the jet generates enough internal Faraday rotation to allow larger values of γ_l therefore relaxing the constraint on γ_l found by Wardle et al. (1998). In the model for component D explored here, a similar ambiguity exists for the value of γ_l. All of our plausible models have $\gamma_l \leqslant 10$; however, this constraint on γ_l is driven by the need to generate enough internal Faraday rotation and depolarization by the relativistic plasma itself and the addition of thermal matter to the jet would relax this constraint on γ_l. Our models for components 5 and 4 provide separate limits of $5 \lesssim \gamma_l \lesssim 35$, based on Faraday conversion, that are not subject to this ambiguity. Taken together, the uncertainties in the value of $B_\perp$ and γ_l allow for smaller values of F_E, perhaps an order of magnitude smaller than that calculated by Wardle et al. (1998).

4.2.3. Uniqueness of Our Model

The model described for component D in the previous sections is of an inhomogeneous jet which is dominated by vector-ordered, poloidal field along the jet axis. In this model, the poloidal magnetic field is responsible for generating the observed circular polarization as intrinsic circular polarization, and the same field provides the internal Faraday rotation and depolarization which produces the relatively low levels of observed linear polarization with a distinctly rotated EVPA which is offset from the jet axis. The inhomogeneous nature of the component explains the Stokes I spectrum, the circular polarization spectrum, and the approximately flat spectrum for the fractional linear polarization and its EVPA, despite the large Faraday depth required. It is these properties that we consider to be robust aspects of our model, and they lead naturally to our constraints on the composition of the radiating particles as parameterized by lepton number ℓ.

We expect that the details of the inhomogeneous model we have used are not unique, and that other inhomogeneous models could reproduce our observations just as well if they have the essential properties listed above. Indeed, as discussed in Section 3.4.2, any inhomogeneous model with smoothly varying magnetic field and particle densities is itself an idealization of the base of the jet which likely has local variations in these properties. In this respect, we see our detailed numerical results from Section 3.4.2 only as estimations of the physical properties of this feature.

Finally, we reiterate that if an external Faraday screen is responsible for rotating and depolarizing the linear polarization, a wider range of general magnetic field and particle models could produce the observed circular polarization. Parsec-scale Faraday rotation measure observations of 3C 279 have been published by Taylor (1998, 2000) and Zavala & Taylor (2001, 2003, 2004) spanning five epochs from early-1997 through mid-2001. Their results agree with ours in that they find consistently negative, but variable, Faraday rotations in the core region of magnitudes encompassing those we see in components D, 5, and 4. The variable rotation measures they observe fit naturally into our model where the amount of poloidal magnetic field drops off sharply from the core region, and newly emerging components can sample a range of internal rotation measures as they propagate down the jet. However, an external screen, very

[8] Note that the dependence of B on ℓ is further complicated by the fraction of uniform field, f_u, such that the quantity $f_u \ell B^{0.5}$ is approximately constant for f_u near unity; however, as f_u is already $\geqslant 0.7$ not much additional reduction in ℓ can be gained by increasing f_u.

close to the jet, could also have these properties. Further out in the jet, these authors find a strong jet component to have a small amount of negative Faraday rotation at about 3 mas from the core in their 1997 and 1998 epochs; however, by 2000, this component shows a small amount of positive Faraday rotation, less than +50 rad m^{-2} in the observer's frame of reference. This shift to positive rotation measure could be related to a collision and re-alignment event this component underwent in mid-1998 (Homan et al. 2003), or the component could simply be far enough from the central engine that other external Faraday screens between us and the source are playing the dominant role.[9]

This evidence indicates that the negative Faraday rotation observed near the core region by ourselves and others is indeed produced local to the jet. It could be due to the fields internal to the jet, as we propose here. Alternatively, it could be generated externally, but close to the jet, by fields and particle densities which scale with frequency and position in just the right way to produce both the approximately constant fractional linear polarization *and* offset EVPA observed in component D at all frequencies. We regard the fact that linear polarization of this kind comes out naturally from the internal rotation model as strong evidence in favor of it.

4.3. Comparison to Integrated UMRAO Monitoring

An interesting result from the integrated UMRAO monitoring of 3C 279 at 4.8, 8.0, and 14.5 GHz is that 3C 279 shows occasional sign reversals in its circular polarization at 4.8 GHz but not at higher frequencies (Aller et al. 2006; and Figure 5). An important question is whether these sign reversals can be understood in the context of the model of the core region preferred for the VLBA data. From Figure 6 it is clear that the core region flux at 4.8 GHz is dominated by components 5 and 4. The Faraday conversion models preferred for components 5 and 4 will naturally produce negative circular polarization at high optical depths, at a frequency about one-third of the spectral turnover (Jones & O'Dell 1977). With spectral turnovers near 9.0 GHz, components 5 and 4 should not be producing negative circular polarization at 4.8 GHz in the VLBA epoch investigated here, and indeed negative circular polarization is not observed near this epoch; however, when these components were first originating near the base of the jet, they must have been more compact with higher turnover frequencies and may well have generated the negative circular polarization observed at 4.8 GHz in mid-2005 along with the increase in Stokes *I* at that time. Strong negative circular polarization is also seen at 4.8 GHz at several other epochs during this period: early-2004, mid-2004, mid-2006, late-2006, and late-2007. Each of these events also appear to be linked with increases in Stokes *I*, suggesting that new components may be ejected from the base of the jet at these times.

5. CONCLUSIONS

We have made multifrequency, parsec-scale observations of the core region of 3C 279 in Stokes *I*, linear polarization, and circular polarization. The core region of 3C 279 consists of three main components: two homogeneous components, 5 and 4, and the inhomogeneous component D at the base of the jet, and we have modeled the full polarization spectra of these components with radiative transfer simulations to constrain the magnetic field and particle properties of the parsec-scale jet in 3C 279.

We find that the polarization properties of the core region, including the amount of linear polarization, the amount and sign of Faraday rotation, and the amount and sign of circular polarization can be explained by a consistent physical model. The base of the jet, component D, is modeled as a conical inhomogeneous Blandford–Königl style jet (Blandford & Königl 1979; Königl 1981). The magnetic field of this feature is dominated by vector-ordered poloidal magnetic field along the jet axis, and we estimated the net magnetic flux of this field. This poloidal field at the base of the jet produces intrinsic circular polarization and depolarizes and rotates the linear polarization. In the homogeneous components 5 and 4, further down the jet, the magnetic field is dominated by local shocks, and a much smaller fraction of vector-ordered, poloidal field remains along the jet axis. This remaining vector-ordered field provides a consistent internal Faraday rotation, which allows Faraday conversion to generate the appropriate amount and spectra of circular polarization from these components.

We note that this physical model is not unique if one allows the observed Faraday rotation and depolarization to occur in screens external to the jet. Such external screens would decouple the linear and circular polarization and allow a wider range of physical parameters; however, we find the fact that all of the essential polarization characteristics can be simultaneously produced by magnetic field and plasma properties internal to the jet itself to be compelling motivation for this model.

With this model, we can additionally constrain the particle properties of the jet. We find the jet to be kinetically dominated by protons with a lepton number $\ell \gtrsim 0.5$ corresponding to $\gtrsim$75% of the radiating particles being electrons, and therefore we cannot rule out a significant admixture of positrons. Based on the amounts of Faraday conversion deduced for the homogeneous components 5 and 4, we find a plausible range for the lower cutoff in the relativistic particle energy spectrum to be $5 \lesssim \gamma_l \lesssim 35$.

We thank Arieh Königl and Nektarios Vlahakis for helpful conversations. This research was supported by an award from Research Corporation, NSF grants AST-0707693, AST-0607523, and AST-0406923, and by funds from the University of Michigan. We thank the referee for insightful comments that have helped us clarify our methods and results.

APPENDIX

OPACITY EFFECTS ON LINEAR POLARIZATION

Here we explore the effect of optical depth, τ, on the observed fraction of linear polarization, m_l, from a partially ordered magnetic field. Our goal is to obtain an analytic model for m_l as a function of τ which can be used in fitting spectra of homogeneous synchrotron sources. We take the ordered part of the magnetic field to be in the plane of the sky at a position angle of 90° so that the emitted linear polarization is entirely Stokes *Q*. We also assume no internal Faraday rotation or conversion. Under these circumstances, the equations of radiative transfer reduce to the following expressions (e.g., Jones 1988).

[9] Note that Zavala & Taylor (2004) find an integrated rotation measure of +31 rad m^{-2} for 3C 279 which is nearly an order of magnitude smaller than even the smallest negative rotation measure we find here for component 4, and thus correction for this integrated value would have essentially no impact on our results.

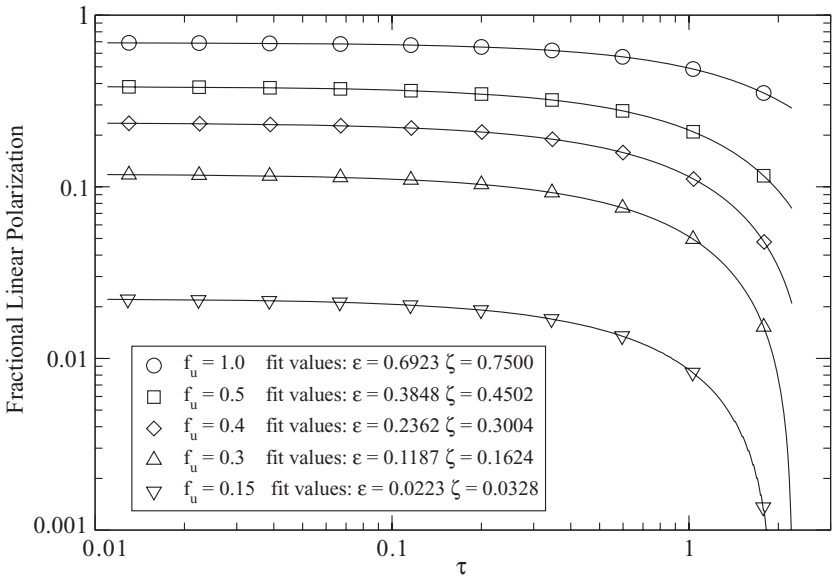

Figure A1. Fractional linear polarization plotted against optical depth from our radiative transfer simulation for a partially ordered magnetic field. The magnetic field is taken to be in the plane of the sky with fractional order given by the parameter f_u described in Section 3.2. The results of the simulation are plotted as open symbols. A fit to the analytical expression given by Equation (A3) is plotted as a solid line for each simulation, and the fitted values for ϵ and ζ appear in the figure legend.

For a completely ordered magnetic field, we have the exact differential equations

$$\frac{dI}{d\tau} + I + \zeta_Q Q = J,$$
$$\frac{dQ}{d\tau} + Q + \zeta_Q I = \epsilon_Q J, \tag{A1}$$

where $\epsilon_Q = 0.6923$ and $\zeta_Q = 0.7500$ are the emission and absorption coefficients, respectively, for $\alpha = -0.5$. For optically thin emission in a completely ordered magnetic field, the fractional linear polarization is equal to the emission coefficient: $m_l(\tau = 0) = \epsilon_Q$.

For a partially ordered field, we will substitute appropriately scaled emission and absorption coefficients, ϵ and ζ, for ϵ_Q and ζ_Q, respectively:

$$\frac{dI}{d\tau} + I + \zeta Q = J;$$
$$\frac{dQ}{d\tau} + Q + \zeta I = \epsilon J. \tag{A2}$$

The scaled emission coefficient ϵ must give the observed fractional linear polarization at $\tau = 0$, so $\epsilon = m_l(\tau = 0)$, and we can guess that the appropriate scaling for the absorption coefficient is similar. We parameterize $\zeta = \zeta_Q \left(\frac{m_l(\tau=0)}{\epsilon_Q}\right)^\eta$, where η is an unknown power, likely to be close to unity.

These coupled, first-order differential equations can be easily solved and we find the resulting fractional linear polarization as a function of opacity:

$$m_l = \frac{Q}{I} = \frac{(1+\epsilon)(1-\zeta)(1-e^{-(1+\zeta)\tau}) - (1-\epsilon)(1+\zeta)(1-e^{-(1-\zeta)\tau})}{(1+\epsilon)(1-\zeta)(1-e^{-(1+\zeta)\tau}) + (1-\epsilon)(1+\zeta)(1-e^{-(1-\zeta)\tau})}. \tag{A3}$$

In the limit $\tau \to 0$, $m_l = \epsilon$ as we expect, and as $\tau \to \infty$, $m_l = \frac{\epsilon-\zeta}{1-\zeta\epsilon}$. All of these expressions are exact for a completely ordered magnetic field; however, we are interested in a partially ordered field using the scaled versions of the emission and absorption coefficients given above: $\epsilon = m_l(\tau = 0)$ and $\zeta = \zeta_Q \left(\frac{m_l(\tau=0)}{\epsilon_Q}\right)^\eta$.

To test these expressions, we ran the radiative transfer simulation described in Section 3.2 with $\alpha = -0.5$ for various fractions, f_u, for the vector-ordered magnetic field, taken to be in the plane of the sky. We used $N = 10^6$ cells along the line of sight to minimize any net contribution from the random component of magnetic field in each cell. We also set the lepton number $\ell = 10^{-5}$ to eliminate the effects of internal Faraday rotation. The fractional polarization, m_l from these runs is plotted against optical depth, τ, in Figure A1. The model given in Equation (A3) is plotted for each value of f_u where the best values of ϵ and ζ were found by a least-squares fit. The best-fit values for ϵ and ζ are given in the legend of Figure A1, and we can see that indeed $\epsilon = m_l(\tau = 0)$ as expected, and we find that our scaled value for $\zeta = \zeta_Q\left(\frac{m_l(\tau=0)}{\epsilon_Q}\right)^\eta$ is an excellent approximation if $\eta = 0.86$.

An additional factor to consider is the possibility of depolarization due to internal Faraday rotation. Burn (1966) predicts additional depolarization of $\sin(\Phi)/\Phi$ where $\Phi_{\rm Burn} = 2.0\Delta\chi$; however, this is for a purely optically thin case. Figure A2 shows the results of our radiative transfer simulation with $f_u = 0.3$ with the jet oriented at $\theta = 45^\circ$ to the line of sight to generate internal Faraday rotation. The amount of Faraday rotation as a function of optical depth was chosen to be similar to what we observe for components 5 and 4, with $\lesssim 40^\circ$ of internal rotation up to an optical depth of $\tau \sim 1$. Note that the internal rotation is well fit by a λ^2 regression up to $\Delta\chi \simeq 40^\circ$. Figure A2(b) of this figure shows the additional effect of internal depolarization beyond the pure optical depth reduction to m_l. To include the effect of internal Faraday depolarization in these plots, we used the linear regression fit to $\Delta\chi = RM\lambda^2$ to produce the Φ values. Note that $\Phi_{\rm Burn}$ somewhat overpredicts the effect of internal depolarization, and we found that a modified factor $\Phi = 1.7\Delta\chi$ produced a better match to the simulation data.

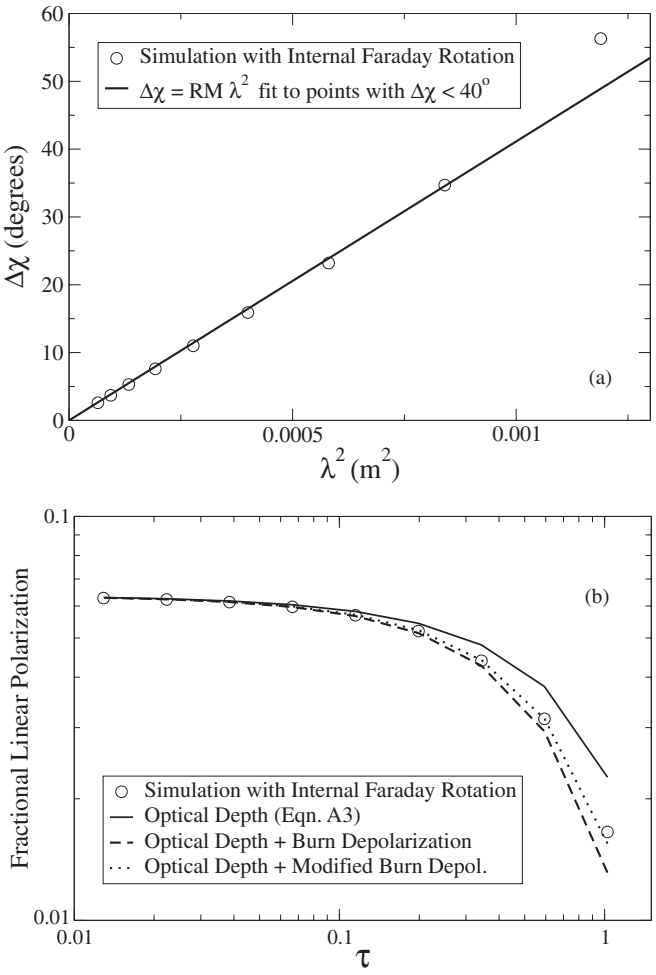

Figure A2. Panel (a) is observed polarization position angle from our radiative transfer simulation with a partially ordered field and internal Faraday rotation. The overplotted line is a linear regression to all of the points with total rotation less than 40°. Panel (b) plots fractional linear polarization against optical depth from the same simulation for all points with total rotation less that 40°. The overplotted lines are the effects of pure optical depth (solid line), optical depth plus Burn style depolarization (dashed line), and optical depth plus the modified Burn depolarization described in the text (dotted line).

Taken together, Equation (A3) and above depolarization rule for internal Faraday rotation, allow us to include fractional linear polarization, m_l, in our analytical fit to the observed Stokes I spectrum of homogeneous jet components to find their peak frequency. To test this technique, we ran this procedure on a detailed numerical simulation of component 5 from our radiative transfer program. We took the results of this simulation at each frequency and treated them as data with the same uncertainties on m_l and Stokes I as the real data from component 5. The simulation had $f_u = 0.05$ with the jet oriented at $\theta = 1.^\circ5$ to the line of sight with a bulk Lorentz factor of $\Gamma = 15$. To generate the right amount of fractional linear polarization at high frequency, a shock of strength $k = 0.64$ was applied and the lower cutoff to the electron energy spectrum was set to $\gamma_l = 19$ to generate the observed amount of Faraday rotation at each frequency. The observed peak frequency of the component was set to be $\nu_{\rm peak} = 8.95$ GHz with a spectral index of $\alpha = -0.50$. We then ran Stokes I and m_l values from this simulation through our analytical peak fitting program and found $\nu_{\rm peak} = 8.80$ GHz with $\alpha = -0.49$, only 2% less than the input values of the simulation.

REFERENCES

Aller, H. D., Aller, M. F., & Hughes, P. A. 2006, BAAS, 38, 1226
Aller, H. D., Aller, M. F., & Plotkin, R. M. 2003, Ap&SS, 288, 17
Asada, K., Inoue, M., Kameno, S., & Nagai, H. 2008, ApJ, 675, 79
Asada, K., Inoue, M., Uchida, Y., Kameno, S., Fujisawa, K., Iguchi, S., & Mutoh, M. 2002, PASJ, 54, L39
Attridge, J. M., Wardle, J. F. C., & Homan, D. C. 2005, ApJ, 633, L85
Beckert, T., & Falcke, H. 2002, A&A, 388, 1106
Begelman, M. C., Blandford, R. D., & Rees, M. J. 1984, Rev. Mod. Phys., 56, 255
Blandford, R. D., & Königl, A. 1979, ApJ, 232, 34
Blandford, R. D., & Payne, D. G. 1982, MNRAS, 199, 883
Blandford, R. D., & Znajek, R. L. 1977, MNRAS, 179, 433
Bower, G. C., Falcke, H., & Backer, D. C. 1999, ApJ, 523, L29
Bower, G. C., Falcke, H., & Mellon, R. R. 2002, ApJ, 578, L103
Brunthaler, A., Bower, G. C., Falcke, H., & Mellon, R. R. 2001, ApJ, 560, L123
Burn, B. J. 1966, MNRAS, 133, 67
Celotti, A., & Fabian, A. C. 1993, MNRAS, 264, 228
De Young, D. S. 2006, ApJ, 648, 200
Fender, R. P., Rayner, D., McCormick, D. G., Muxlow, T. W. B., Pooley, G. G., Sault, R. J., & Spencer, R. E. 2002, MNRAS, 336, 39
Fender, R., Rayner, D., Norris, R., Sault, R. J., & Pooley, G. 2000, ApJ, 530, L29
Fendt, C. 2006, ApJ, 651, 272
Gabuzda, D. C., Murray, É., & Cronin, P. 2004, MNRAS, 351, L89
Gabuzda, D. C., Vitrishchak, V. M., Mahmud, M., & O'Sullivan, S. P. 2008, MNRAS, 384, 1003
Gómez, J. L., Marscher, A. P., Jorstad, S. G., Agudo, I., & Roca-Sogorb, M. 2008, ApJ, 681, L69
Homan, D. C., Attridge, J. M., & Wardle, J. F. C. 2001, ApJ, 556, 11
Homan, D. C., & Lister, M. L. 2006, AJ, 131, 1262
Homan, D. C., Lister, M. L., Kellermann, K. I., Cohen, M. H., Ros, E., Zensus, J. A., Kadler, M., & Vermeulen, R. C. 2003, ApJ, 589, L9
Homan, D. C., Ojha, R., Wardle, J. F. C., Roberts, D. H., Aller, M. F., Aller, H. D., & Hughes, P. A. 2001, ApJ, 549, 840
Homan, D. C., Ojha, R., Wardle, J. F. C., Roberts, D. H., Aller, M. F., Aller, H. D., & Hughes, P. A. 2002, ApJ, 568, 99
Homan, D. C., & Wardle, J. F. C. 1999, AJ, 118, 1942
Homan, D. C., & Wardle, J. F. C. 2000, ApJ, 535, 575
Homan, D. C., & Wardle, J. F. C. 2003, Ap&SS, 288, 29
Homan, D. C., & Wardle, J. F. C. 2004, ApJ, 602, L13
Jones, T. W. 1988, ApJ, 332, 678
Jones, T. W., & O'Dell, S. L. 1977, ApJ, 214, 522
Jorstad, S. G., Marscher, A. P., Lister, M. L., Stirling, A. M., Cawthorne, T. V., Gómez, J.-L., & Gear, W. K. 2004, AJ, 127, 3115
Koide, S., Shibata, K., Kudoh, T., & Meier, D. L. 2002, Science, 295, 1688
Komesaroff, M. M., Roberts, J. A., Milne, D. K., Rayner, P. T., & Cooke, D. J. 1984, MNRAS, 208, 409
Königl, A. 1981, ApJ, 243, 700
Laing, R. A., & Bridle, A. H. 2002, MNRAS, 336, 328
Laing, R. A., Canvin, J. R., & Bridle, A. H. 2006, Astron. Nachr., 327, 523
Lister, M. L., & Homan, D. C. 2005, AJ, 130, 1389
Liu, Y., Jiang, D. R., & Gu, M. F. 2006, ApJ, 637, 669
Macquart, J.-P., Kedziora-Chudczer, L., Rayner, D. P., & Jauncey, D. L. 2000, ApJ, 538, 623
Marscher, A. P. 1987, in Superluminal Radio Sources, ed. J. A. Zensus & T. J. Pearson (Cambridge: Cambridge Univ. Press), 280
Marscher, A. P., Jorstad, S. G., Gómez, J.-L., Aller, M. F., Teräsranta, H., Lister, M. L., & Stirling, A. M. 2002, Nature, 417, 625
Marscher, A. P., et al. 2008, Nature, 452, 966
Meier, D. L., Koide, S., & Uchida, Y. 2001, Science, 291, 84
Rayner, D. P., Norris, R. P., & Sault, R. J. 2000, MNRAS, 319, 484
Ruszkowski, M., & Begelman, M. C. 2002, ApJ, 573, 485
Sault, R. J., & Macquart, J.-P. 1999, ApJ, 526, L85
Shepherd, M. C. 1997, in ASP Conf. Ser. 125, Astronomical Data Analysis Software and Systems VI, ed. G. Hunt & H. E. Payne (San Francisco, CA: ASP), 77
Sikora, M., & Madejski, G. 2000, ApJ, 534, 109
Taylor, G. B. 1998, ApJ, 506, 637
Taylor, G. B. 2000, ApJ, 533, 95
Vlahakis, N., & Königl, A. 2004, ApJ, 605, 656
Wang, J.-M., Luo, B., & Ho, L. C. 2004, ApJ, 615, L9

Wardle, J. F. C., Cawthorne, T. V., Roberts, D. H., & Brown, L. F. 1994, ApJ, 437, 122
Wardle, J. F. C., & Homan, D. C. 2003, Ap&SS, 288, 143
Wardle, J. F. C., Homan, D. C., Ojha, R., & Roberts, D. H. 1998, Nature, 395, 457
Woo, J.-H., & Urry, C. M. 2002, ApJ, 581, L5
Zavala, R. T., & Taylor, G. B. 2001, ApJ, 550, L147
Zavala, R. T., & Taylor, G. B. 2003, ApJ, 589, 126
Zavala, R. T., & Taylor, G. B. 2004, ApJ, 612, 749
Zavala, R. T., & Taylor, G. B. 2005, ApJ, 626, L73